Received: 27 November 2021 | Revised: 20 February 2022 | Accepted: 22 February 2022

DOI: 10.1002/nme.6967

RESEARCH ARTICLE

WILEY

A *p*-adaptive, implicit-explicit mixed finite element method for diffusion-reaction problems

Mebratu F. Wakeni[1] | **Ankush Aggarwal**[1] | **Łukasz Kaczmarczyk**[1] | **Andrew T. McBride**[1] | **Ignatios Athanasiadis**[1] | **Chris J. Pearce**[1] | **Paul Steinmann**[1,2]

[1]Glasgow Computational Engineering Centre, James Watt School of Engineering, University of Glasgow, Glasgow, UK

[2]Institute of Applied Mechanics, Friedrich-Alexander, University of Erlangen-Nuremberg, Erlangen, Germany

Correspondence
Łukasz Kaczmarczyk, Glasgow Computational Engineering Centre, James Watt School of Engineering, University of Glasgow, Glasgow G12 8QQ, UK.
Email: lukasz.kaczmarczyk@glasgow.ac.uk

Abstract

A new class of implicit-explicit (IMEX) methods combined with a *p*-adaptive mixed finite element formulation is proposed to simulate the diffusion of reacting species. Hierarchical polynomial functions are used to construct a conforming base for the flux vectors, and a non-conforming base for the mass concentration of the species. The mixed formulation captures the distinct nonlinearities associated with the flux constitutive equations and the reaction terms. The IMEX method conveniently treats these two sources of nonlinearity implicitly and explicitly, respectively, within a single time-stepping framework. A reliable *a posteriori* error estimate is proposed and analyzed. A *p*-adaptive algorithm based on the proposed *a posteriori* error estimate is also constructed. The combination of the proposed residual-based *a posteriori* error estimate and hierarchical finite element spaces allows for the formulation of an efficient *p*-adaptive algorithm. A series of numerical examples demonstrate the performance of the approach for problems involving travelling waves, and possessing discontinuities and singularities. The flexibility of the formulation is illustrated via selected applications in pattern formation and electrophysiology.

KEYWORDS

diffusion-reaction, *h*- and *p*-adaptivity, hierarchical basis functions, implicit-explicit method, mixed formulation

1 | INTRODUCTION

1.1 | Motivation

The spatio-temporal dynamics of multiple species interacting through a combination of two distinct mechanisms, namely reaction and diffusion, can be described by *diffusion-reaction* equations. Reaction refers to the inter/intra species interactions, resulting in the production and extinction of species. It is embodied in a term that is referred to as *reaction kinetics* f, which is a function of the mass concentration(s) m of the involved species. Diffusion refers to the flow of substance (concentration) in space, and is mathematically described by a flux $\boldsymbol{h}$ related to m (and/or its spatial gradient) through a constitutive equation. Diffusion-reaction models are relevant in various important

applications, including tissue morphogenesis and pattern formation,[1,2] tissue remodeling,[3-7] electrophysiology,[8,9] and epidemiology.[10]

The aforementioned applications motivate the need for robust and efficient numerical methods for solving diffusion-reaction problems. Various numerical methods have been proposed for approximating the solutions of these problems. Meshless methods in conjunction with operator-splitting techniques have been used in in one- and two-dimensions.[11] Olmos and Shizgal[12] solved Fitzhugh–Nagumo type models using a multidomain algorithm based on a pseudospectral approach. A review of some finite-difference-based methods in one-dimension can be found in Ramos.[13] Furthermore, a finite difference scheme was constructed for the simulation of waves in excitable media using a two-variable diffusion-reaction equation.[14] However, finite difference and spectral algorithms are suitable only for approximations over relatively simple domains.

1.2 | Spatial discretization

The finite element method (FEM), due to its capabilities in handling arbitrary geometry and nonlinearities and its strong theoretical foundation, is a natural choice for solving diffusion-reaction problems. The majority of the finite element numerical approaches for diffusion-reaction problems presented in the literature are based on the standard, single-field formulation. Ruiz-Baier[15] employed the standard formulation in a computational framework for the coupling of diffusion-reaction and elasticity. Tuncer et al.[16] used a projected finite element approach for stationary, closed surface geometries to simulate pattern-formation in biological applications. MacDonald et al.[17] constructed a moving mesh FEM for simulating chemotaxis in two-dimensions. A multigrid FEM on stationary and evolving surfaces was proposed by Landsberg and Voigt.[18] A semi-linear multistep finite element was constructed in Mergia and Patidar[19] for the two-dimensional simulation of pattern formation in ecological application. Mackenzie et al.,[20] recently proposed an interesting finite element scheme for diffusion-reaction equations on evolving domains wherein a H^1-conserving FEM is combined with an arbitrary Lagrangian Eulerian (ALE) formulation, which leads to a globally mass-conserving property.

Solutions of diffusion-reaction problems exhibit a variety of phenomena from the formation of travelling waves to complex structures like dissipative solitons. Some solutions may even involve low regularity features such as evolving jump discontinuities and singularities. The H^1-conforming basis functions used in the standard formulation impose an unnecessarily high regularity requirement. Mixed FEMs see for example[21-23]offer an elegant solution for such problems. Mixed FEMs are two-field formulations, which employ a $H(\mathrm{div})$-conforming basis for the flux and an L^2-conforming basis for the mass concentration. This combination of basis functions relaxes the conformity requirements, allowing a wider class of solutions to be approximated accurately. Furthermore, the mixed method allows the nonlinearities that may appear in the flux constitutive equation and the reaction term to be considered separately.

Numerical studies of diffusion-reaction type problems using mixed methods are, by comparison to standard formulations, relatively few. In Fu et al.,[24] a stabilized mixed formulation was proposed for solving steady and unsteady diffusion-reaction problems. In this approach, H^1-conforming finite element spaces are used for m, and L^2-conforming spaces for $\boldsymbol{h}$. With regard to the finite element space used for m, such a method has no particular advantage over the standard FEM in terms of accuracy. Recently, Liu et al.[25] proposed and analyzed a mixed-type finite element formulation based on minimization of a functional which accounts for the flux jump across control volume boundaries subject to local conservation of mass. The finite element spaces are composed of standard conforming shape functions for the primary field and piecewise constant functions over the control volume boundaries for the Lagrange multiplier. Kadeethum et al.[26] recently proposed a mixed, enriched finite element framework for hydro-mechanical-chemical processes. They also demonstrated that the computational framework provides local mass conservation for various strongly heterogeneous and anisotropic materials.

Adaptive schemes are particularly important for problems involving the movement of fine features such as travelling waves. A reliable and efficient *a posteriori* error estimate is essential for the success of such a scheme. Most of the recent developments in this respect, however, have focused particularly on the time-independent case, see for example[27-32]. In Chaudhry et al.,[33] an adjoint-based *a posteriori* analysis for estimation of error for advection-diffusion-reaction problems is presented. Bériot et al.[32] proposed a *hp*-adaptive, spectral, discontinuous Galerkin method for the incompressible Navier–Stokes equation. For time-dependent problems, Chalmers et al.[34]

developed a *hp*-adaptive, spectral, discontinuous Galerkin method. Other important works on robust *a posteriori* error indicators include.[35,36]

1.3 | Temporal discretization

Most numerical procedures for diffusion-reaction equations that utilize finite elements, approach the temporal integration using either fully-implicit or fully-explicit methods. It is well-established that explicit methods can be very efficient and are easy to implement. However, they usually suffer in terms of algorithmic stability, and impose severe time step restrictions arising from the diffusion term. Implicit methods are known for their greater stability, but can be challenging in terms of implementation, and are usually less efficient as they lead to the solution of a large system of algebraic equations. In addition, for nonlinear problems, it is necessary to derive and compute tangent matrices that includes implicit nonlinearities at each time step, adding further inefficiencies. Implicit-explicit (IMEX) methods mitigate such problems by combining the advantages of explicit and implicit methods.[37] By treating the non-local diffusion term (involving a spatial derivative) implicitly, and the local reaction term (without a spatial derivative) explicitly, one can eliminate the coupling effect of spatial mesh size h and the time step size Δt on the stability condition. This allows the spatial mesh to be refined adaptively without the need for reducing the time-step size. In the literature, IMEX methods have continued to be used in various context, for example, they have recently been used for convection-diffusion-reaction[33,38-40] and Navier–Stokes[34,41,42] equations. In Meng et al.,[41] a fractional-step algorithm for an incompressible Navier–Stokes equation on moving overlapping meshes has been proposed. The predictor step in the fractional-step algorithm involves solving an equation which is essentially a convection-diffusion equation using an IMEX scheme in which the diffusion part is treated implicitly in order to ensure that the time step restriction remains $\Delta t \propto h$. This is important for adaptive schemes where the diffusion term becomes dominantly stiff due to -refinement. In DeCaria and Schneier,[42] a stability and convergence analysis of variable time-step size IMEX schemes with mixed FEMs for the incompressible Navier–Stokes equation has been performed. A time adaptive algorithm that combines solution of the IMEX method with a time filter correction (as a postprocessing step) has also been proposed.

1.4 | Contribution of the work

In this article, we propose a *p*-adaptive, mixed FEM with IMEX temporal integration for a general class of diffusion-reaction problems. We extend the *a posteriori* error estimates of the mixed formulation for linear elliptic problems proposed in Braess and Verfurth[43] to the transient diffusion-reaction framework. An upper bound to the energy error norm based on the *a posteriori* error estimator is derived and proved. An efficient *p*-adaptive strategy which capitalizes on the hierarchical features of the basis functions as well as straightforward calculations of the *a posteriori* error estimator is proposed, see also [32]. It is known that on elements with higher polynomial order basis functions the diffusion term becomes dominantly more stiff than the reaction term.[41] In addition, the absence of spatial derivatives in the reaction term means that there is no coupling of the mesh size h and the time step size Δt as a result of the spatio-temporal discretization of the reaction term. These motivates the choice the IMEX approach such that the flux constitutive equation is treated implicitly, while, the nonlinearities in the reaction term are handled explicitly. Several numerical examples are presented that demonstrate the performance of the present numerical method in different areas including pattern-formation and electrophysiology.

1.5 | Manuscript organization

The article is organized as follows. In Section 2, a general mathematical model of multi-species diffusion-reaction systems is presented briefly. The weak formulation of the model using a mixed approach is described in Section 3. In Section 4, relevant aspects of the numerical procedure for the temporal discretization using the IMEX method and the spatial approximation using mixed Galerkin approaches are presented. Finally, in Section 7 the performance and capabilities of the proposed formulations are demonstrated using various numerical examples. Here, the performance of the mixed and the standard formulations are compared, and finally some selected examples relevant to pattern formation, ecology and electrophysiology are simulated using the mixed method.

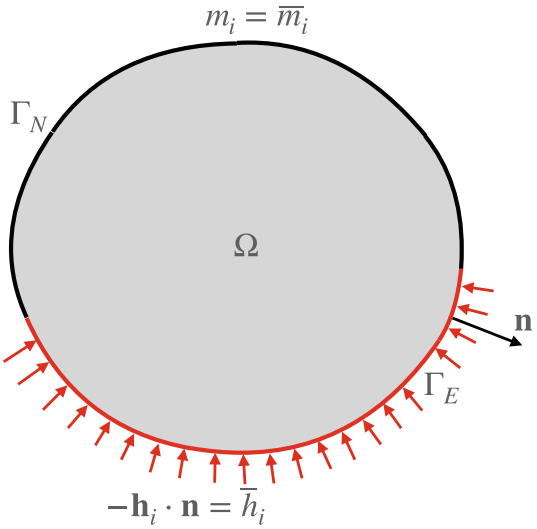

FIGURE 1 Schematic of the domain Ω with boundary partitions Γ_E and Γ_N

2 | MODEL OVERVIEW

Consider n species, each with mass concentration m_i, where $i = 1, 2, 3, \ldots, n$, interacting in an open, bounded region $\Omega \subset \mathrm{I\,R}^d$ ($d = 1, 2,$ or 3). The local form of the mass balance, for each of the species, is given by

$$\dot{m}_i + \operatorname{div} \boldsymbol{h}_i = f_i(m_1, \ldots, m_n), \qquad i = 1, \ldots, n, \tag{1}$$

where $\boldsymbol{h_i}$ denotes the concentration flux of the i^{th} species, and f_i is the chemical kinetics term that represents the rate of production or degradation of species concentration of the i^{th} species as a result of its interaction with other species. In addition to the mass balance Equation (1), a constitutive relation relating the flux $\boldsymbol{h}_i$ to the mass concentration m_i is required. A commonly used constitutive relation is given by

$$\boldsymbol{h}_i = -\boldsymbol{D}_i \nabla\, m_i, \qquad i = 1, \ldots, n. \tag{2}$$

Here $\boldsymbol{D}_i$ is a symmetric and positive-definite second-order tensor representing a potentially spatially varying diffusivity/mobility of the i^{th} species on the domain Ω. Let Γ_N and Γ_E be nonoverlapping portions of the boundary of Ω, denoted by Γ (see Figure 1), such that $\overline{\Gamma_N \cup \Gamma_E} = \Gamma$. The prescribed boundary conditions imposed on these partitions are

$$m_i = \overline{m}_i \qquad \text{on } \Gamma_N, \text{ and} \tag{3}$$

$$-\boldsymbol{h}_i \cdot \boldsymbol{n} = \overline{h}_i \qquad \text{on } \Gamma_E, \tag{4}$$

where $\boldsymbol{n}$ represents the unit outward normal vector to the boundary Γ. A complete description of the problem also requires the prescription of initial conditions for each m_i, which read as

$$m_i(\boldsymbol{x}) = m_i^0(\boldsymbol{x}), \qquad \text{at } t = 0, \quad \forall \boldsymbol{x} \in \Omega.$$

3 | WEAK FORMULATIONS

The focus here is on the mixed formulation. However, for the sake of completeness, the standard, single-field formulation is first briefly stated. Thereafter, a detailed presentation of the mixed formulation and its spatial and temporal discretization is given.

In the context of initial-boundary value problems, such as analyzed here, it is helpful to view functions of space and time as mappings from the time interval of interest $\mathbb{I} = [0,\ T]$ to the corresponding functional space. For example, a function $u \in L^2(\Omega; \mathbb{I})$ is understood as the map $u : \mathbb{I} \to L^2(\Omega)$ ($L^2(\Omega)$ denotes the space of measurable functions which are square integrable over the domain Ω). In addition to the functional space $L^2(\Omega; \mathbb{I})$ we also make use of the spaces $H^1(\Omega; \mathbb{I})$ and $H(\mathrm{div}, \Omega; \mathbb{I})$, where

$$H^1(\Omega) = \{m \in L^2(\Omega) : \quad \nabla\, m \in [L^2(\Omega)]^d\}, \quad \text{and}$$
$$H(\mathrm{div}, \Omega) = \{\boldsymbol{h} \in [L^2(\Omega)]^d : \quad \mathrm{div}\, \boldsymbol{h} \in L^2(\Omega)\}.$$

The natural norms endowed by $H^1(\Omega)$ and $H(\mathrm{div}, \Omega)$ are, respectively, given by

$$\|m\|^2_{1,\Omega} := \|m\|^2_{0,\Omega} + \|\nabla\, m\|^2_{0,\Omega}, \text{ and}$$
$$\|\boldsymbol{h}\|^2_{\mathrm{div},\Omega} := \|\boldsymbol{h}\|^2_{0,\Omega} + \|\mathrm{div}\, \boldsymbol{h}\|^2_{0,\Omega},$$

where $\|\cdot\|_{0,\Omega}$ denotes the standard L^2-norm for scalar or vector-valued functions.

For a mixed finite element formulation, in addition to m_i, the flux $\boldsymbol{h}_i$ is taken as an unknown variable. Thus, the constitutive relation (2) is rewritten as

$$\boldsymbol{D}_i^{-1}\boldsymbol{h}_i + \nabla\, m_i = \boldsymbol{0}. \tag{5}$$

The mixed weak form associated with Equations (5) and (1) reads:

find $(\boldsymbol{h}_i,\ m_i) \in H(\mathrm{div}, \Omega; \mathbb{I}) \times L^2(\Omega; \mathbb{I})$ such that

$$a_i(\boldsymbol{\tau},\ \boldsymbol{h}_i) - b(\boldsymbol{\tau},\ m_i) = (\boldsymbol{\tau} \cdot \boldsymbol{n},\ \overline{m}_i)_{\Gamma_N}, \qquad \forall \boldsymbol{\tau} \in H_{0E}(\mathrm{div},\ \Omega), \tag{6}$$
$$\frac{\mathrm{d}}{\mathrm{d}t}\, c(v,\ m_i) + b(\boldsymbol{h},\ v) = \ell_i(v), \qquad \forall v \in L^2(\Omega), \tag{7}$$

where the subspace $H_{0E}(\mathrm{div}, \Omega) \subset H(\mathrm{div}, \Omega)$ possesses a vanishing normal component $\boldsymbol{\tau} \cdot \boldsymbol{n}$ on the boundary Γ_E. Also, the test functions v and $\boldsymbol{\tau}$ are time-independent. In this case, the trial flux solution $\boldsymbol{h}_i$ satisfies the boundary conditions (4) *a priori*, making it an essential boundary condition in the context of the mixed formulation (6) and (7).

The bilinear forms $a_i : H(\mathrm{div}, \Omega) \times H(\mathrm{div}, \Omega) \to \mathrm{I\,R}$, $b : H(\mathrm{div}, \Omega) \times L^2(\Omega) \to \mathrm{I\,R}$, and $c : L^2(\Omega) \times L^2(\Omega) \to \mathrm{I\,R}$ are defined by

$$a_i(\boldsymbol{\tau},\ \boldsymbol{h}_i) := (\boldsymbol{\tau},\ \boldsymbol{D}_i^{-1}\boldsymbol{h}_i)_\Omega,$$
$$b(\boldsymbol{\tau},\ m_i) := (\mathrm{div}\ \boldsymbol{\tau},\ m_i)_\Omega,$$
$$c(m_i,\ v) := (m_i,\ v)_\Omega,$$

for any $\boldsymbol{\tau}, \boldsymbol{h}_i \in H(\mathrm{div}, \Omega)$ and $m_i, v \in L^2(\Omega)$.

Remark

1. When the $L^2(\Omega)$ space of test functions is replaced by its discrete counterpart, the test function v is chosen such that it vanishes everywhere in the domain Ω except on a given element Ω^e. This in turn implies that for v in (7) set to unity on the element Ω^e, one obtains

$$\frac{\mathrm{d}}{\mathrm{d}t}\int_{\Omega^e} m_i\ \mathrm{d}\Omega + \int_{\Omega^e} \mathrm{div}\ \boldsymbol{h}_i\ \mathrm{d}\Omega = \int_{\Omega^e} f_i\ \mathrm{d}\Omega.$$

   As a result, such an approximation method is said to have a locally conservative property. That is, the conservation of mass (1) is satisfied on each element.

2. The classification of boundary conditions in the mixed formulation is opposite to the standard single-field case (see Appendix A). In the standard formulation, the boundary condition (4) is a natural one as it does not require *a priori* prescription on the space of trial or test spaces. By contrast, it becomes an essential boundary condition in the mixed formulation since the trial and test functions require the normal flux at the boundary Γ_E to be prescribed *a priori*. The role of Equation (3) is also reversed, that is, it is essential in the standard formulation but natural in the mixed formulation.

4 | DISCRETIZATION

The temporal discretization of the weak formulations, (6) and (7), using a combination of implicit and explicit methods is now presented. Then, the discrete counterparts of the spaces $H(\mathrm{div}, \Omega)$ and $L^2(\Omega)$ are detailed in the context of the hierarchical construction of shape functions over a triangle/tetrahedral mesh.

4.1 | Temporal discretization

Consider first the temporal discretization of the mixed formulation using a class of IMEX methods. The time interval of interest is partitioned into subintervals $[t_{n-1},\ t_n]$ with step size $\Delta t_n = t_n - t_{n-1}$. Note that the partition need not be uniform, that is, the step-sizes need not be equal. As Equation (6) is without a time derivative, we treat it fully implicitly at the current time t_n. For the IMEX method only the second Equation (7) involving time derivatives is relevant. For clarity of notation, we drop the subscript i from the weak forms (6) and (7), and, in a general multistep context, replace each term by interpolation or extrapolation formulas as linear combinations of previous discrete values, as defined by

$$\frac{\mathrm{d}}{\mathrm{d}t}\, c(\bullet,\ m) \approx \overset{\circ}{c}(\bullet) := \frac{\alpha_r}{\Delta t_n}\, c(\bullet,\ m^n) + \sum_{j=0}^{r-1} \frac{\alpha_j}{\Delta t_n}\, c(\bullet,\ m^{n+j-r}), \tag{8}$$

$$b(\boldsymbol{h},\ \bullet) \approx \hat{b}(\bullet) := \beta_r\, b(\bullet,\ \boldsymbol{h}^n) + \sum_{j=0}^{r-1} \beta_j\, b(\boldsymbol{h}^{n+j-r},\ \bullet), \tag{9}$$

$$\ell(\bullet) \approx \tilde{\ell}(\bullet) := \sum_{j=0}^{r-1} \gamma_j\, \ell^{n+j-r}(\bullet), \tag{10}$$

where $\ell^k(\bullet)$, $k = n-r,\ \dots\ , n-1$, represents the family of functionals $\ell(\bullet)$ defined using the time discrete values of the reaction kinetics $f^k = f(m^k)$, that is, with reference to (A2),

$$\ell^k(v) = (f^k,\ v)_\Omega.$$

The coefficients $\beta_0, \beta_1, \dots, \beta_r$ and $\alpha_0, \alpha_1, \dots, \alpha_r$ correspond to the implicit interpolation formula (corresponding to Equations 8 and 9) for the value and its time derivative of a field at t_n on the time interval $[t_{n-r}, t_n]$. $\gamma_0, \gamma_1, \dots, \gamma_{r-1}$ are coefficients of the explicit extrapolation (corresponding to the Equation 10) of a field at t_n on the interval. The integer r represents the extent to which previous step solutions, starting from the current step, are included in the scheme. Some of the commonly used IMEX schemes are listed in Appendix A.

Substituting the discrete approximations (8)–(10) into the weak formulation (7), together with the discrete equation corresponding to Equation (6) at the current time-step renders

$$a^n(\boldsymbol{\tau}) - b^n(\boldsymbol{\tau}) = (\boldsymbol{\tau}\cdot\boldsymbol{n},\ \overline{m})_{\Gamma_N}, \qquad \forall \boldsymbol{\tau} \in H(\mathrm{div},\ \Omega),\ \text{and} \tag{11}$$

$$\overset{\circ}{c}(v) + \hat{b}(v) = \tilde{\ell}(v), \qquad \forall v \in L^2(\Omega), \tag{12}$$

where

$$a^n(\boldsymbol{\tau}) := a(\boldsymbol{\tau}, \boldsymbol{h}^n), \quad b^n(\boldsymbol{\tau}) := b(\boldsymbol{\tau},\ m^n).$$

Note, (11) and (12) constitute a boundary value problem at the time-step t_n. IMEX methods can be viewed as multistep schemes involving $r-1$ previous time step's solutions. They are formally r^{th}-order convergent in time.

4.2 | Spatial discretization

Assume a regular decomposition $\mathcal{T}_h$ of Ω into simplexes (triangles in 2D and tetrahedrals in 3D). For a given $p \in \mathbb{Z}^+$ (a non-negative integer), denote the set of all polynomials, on a given $T \in \mathcal{T}_h$, whose order is less than or equal to p by $\mathcal{P}_p(T)$. For FEMs which typically involve the use of non-uniform higher-order approximations on unstructured meshes, increasing the order of the polynomial space locally via p- and hp- adaptivity can lead to complications in enforcing global conformity of shape functions.[44] Hierarchical shape functions address such problems, as well as naturally supporting the use of p- and hp-adaptivity.[45,46] The construction of hierarchical shape functions of arbitrary order with various conformity conditions to obtain finite element subspaces for $L^2(\Omega)$, $H^1(\Omega)$, $H(\text{div}, \Omega)$ on a general unstructured meshes is detailed in Ainsworth and Coyle.[44] An alternative construction for $H(\text{div})$ conforming exact sequence elements with arbitrary order has been proposed by Fuentes et al.[47] Note, that the space proposed by Ainsworth and Coyle,[44] consisting of divergence-free zero normal functions, is used for the numerical examples in Section 7.

Here, hierarchic shape functions are used to define the finite element spaces corresponding to the triangulation $\mathcal{T}_h$ such that the test spaces, for concentration m and flux, are defined as

$$\mathcal{S}_h = \{v_h \in L^2(\Omega) : v_h|_T \in \mathcal{P}^{p-1}(T), \text{ where } T \in \mathcal{T}_h\}, \text{ and} \tag{13}$$

$$\mathcal{V}_h^0 = \{\boldsymbol{\tau}_h \in H(\text{div}, \Omega) : \boldsymbol{\tau}_h|_T \in [\mathcal{P}^p(T)]^{dim} \text{ and } \boldsymbol{\tau}_h \cdot \boldsymbol{n} = 0 \text{ on } \Gamma_E\}, \tag{14}$$

where $dim = 1, 2, \text{ or } 3$ refers to the spatial dimension. While the trial space for concentration m is also $\mathcal{S}_h$, the trial space $\mathcal{V}_h$ for the flux $\boldsymbol{h}$ is given by

$$\mathcal{V}_h = \{\boldsymbol{\tau}_h \in H(\text{div}, \Omega) : \boldsymbol{\tau}_h|_T \in [\mathcal{P}^p(T)]^{dim} \text{ and } -\boldsymbol{\tau}_h \cdot \boldsymbol{n} = \overline{h} \text{ on } \Gamma_E\}. \tag{15}$$

It should be noted that to obtain a stable pair $(\boldsymbol{h}_h, m_h)$ the order of approximation for $\mathcal{V}_h$ is required to be at least one order higher than that of $\mathcal{S}_h$, see, for example Reference[21].

For the approximation of $(\boldsymbol{h}, m)$, we employ the finite dimensional trial space $(\mathcal{V}_h, \mathcal{S}_h)$ and test space $(\mathcal{V}_h^0, \mathcal{S}_h)$, as defined in Equations (13)–(15), following a Galerkin approach. Having specified the corresponding finite element spaces, the spatio-temporal discrete form of the Equations (11) and (12) produces a block matrix system given by

$$\begin{bmatrix} \mathbf{K} & \mathbf{B} \\ \mathbf{B}^{\mathrm{T}} & -\sigma\mathbf{M} \end{bmatrix} \begin{bmatrix} \mathbf{H}^n \\ \mathbf{m}^n \end{bmatrix} = \begin{bmatrix} \mathbf{F} \\ \mathbf{G} \end{bmatrix}, \tag{16}$$

where

$$\mathbf{K}_{IJ} = a(\boldsymbol{\tau}_I^h, \boldsymbol{\tau}_J^h), \quad \mathbf{B}_{IL} = -b(\boldsymbol{\tau}_I^h, v_L^h), \text{ and } \mathbf{M}_{KL} = c(v_K^h, v_L^h).$$

Here, I, J denote the global indices corresponding to the numbering of the basis elements of $\mathcal{V}_h$, while K, L correspond to that of $\mathcal{S}_h$. The right hand side contributions $\mathbf{F}$ and $\mathbf{G}$ are given by

$$\mathbf{F}_I = (\boldsymbol{\tau}_I \cdot \boldsymbol{n}, \overline{m}_h)_{\Gamma_E} \qquad \text{and} \quad \mathbf{G}_K = \frac{1}{\beta_r} \sum_{j=0}^{r-1} \left[\gamma_j \, \ell^{n+j-r}(v_K) - \beta_j \, b\left(v_K, \boldsymbol{h}_h^{n+j-r}\right)\right].$$

The vector $\mathbf{H}^n$ and $\mathbf{m}^n$ are the solution vectors containing the degrees-of-freedom (DoF) associated with the current values of $\boldsymbol{h}^n$ and m^n, respectively. The coefficient $\sigma = \alpha_r/[\Delta t_n \, \beta_r]$ is a shift coefficient of the mass matrix $\mathbf{M}$. The matrices $\mathbf{K}$ and $\mathbf{M}$ are positive definite and symmetric. Solvability of the block system (16) also requires that $\mathbf{B}$ as a linear map is surjective (see, for example, Reference[21]Section 3.3). The requirement that the order of the flux shape function should be at least one order higher than the mass concentration shape function is a sufficient condition for the surjectivity of $\mathbf{B}$.

Formally, for sufficiently smooth solutions, the expected rate of convergence for the spatial approximation employing the finite element spaces $\mathcal{S}_h$ and $\mathcal{V}_h$ will be of order p in both the L^2 and the natural norms.

Remark

1. One of the most important implications of the mixed formulation, from a computational perspective, is that the matrix $\mathbf{M}$ can be inverted locally on an element-by-element basis, and the inverse is sparse. This is due to the fact that there is no conformity requirement on $m_h \in \mathcal{S}_h \subset L^2(\Omega)$ over element boundaries.
2. The consequence of the above observation is that one can efficiently solve the block system using a solver that utilizes a Schur complement preconditioner. More precisely, one can exactly compute the sparse Schur complement $\mathbf{S} = \mathbf{K} + \mathbf{B}\mathbf{M}^{-1}\mathbf{B}^{\mathrm{T}}$ in an efficient manner.

5 | *A POSTERIORI* ERROR ESTIMATORS AND *p*-ADAPTIVITY

Adaptive FEMs are a fundamental numerical approach in science and engineering applications. The success of an adaptive algorithm relies on the availability of a good error indicator (or *a posteriori* error estimator) that provides an upper bound to the true approximation error, and the complexity of its implementation and computation. In this section, we present a residual-based error estimate that can be computed cheaply. This estimate together with the hierarchical construction of the shape functions makes the method well suited for local p-adaptivity. Hierarchical shape functions (and DoF) are associated with mesh entities such as vertices, edges, faces, and volumes, rather than nodes. For example, in 2D, if the local order of two adjacent faces F_1 and F_2 sharing an edge E is different, say order-p_1 and order-p_2, respectively, then to satisfy the global $H(\mathrm{div}, \Omega)$-conformity one only needs to add local shape functions of order-$\max(p_1, p_2)$ on the edge E. By contrast, since there is no continuity requirement for $L^2(\Omega)$ along element interfaces, the shape functions are only associated with faces in the 2D case. Thus, the polynomial order of L^2 shape functions can be set independently in each element, thereby greatly simplifying the implementation of p-adaptivity.

To underpin an effective local p-adaptivity scheme, one requires a reliable *a posteriori* error estimate that provides an upper bound to the true error and, at best, decays with the same rate as the true error as the polynomial order increases uniformly. The energy norm on $H(\mathrm{div}, \Omega) \times L^2(\Omega)$, defined by

$$\|\boldsymbol{h}\|_{\mathrm{div},\Omega} + \|m\|_{0,\Omega}, \tag{17}$$

is the appropriate norm for measuring the magnitude of approximation errors in the mixed formulation (6) and (7).

To develop the error estimator, and for the sake of simplicity, we shall consider a one-species mixed transient problem with homogeneous boundary condition on $m_{h,q}$, where the additional subscript used here is to denote the order of the polynomial space, that is

$$a(\boldsymbol{\tau}_{h,p},\ \boldsymbol{h}^n_{h,p}) - b(\boldsymbol{\tau}_{h,p},\ m^n_{h,p-1}) = 0 \qquad \forall \boldsymbol{\tau}_{h,p} \in \mathcal{V}_{h,k}, \tag{18}$$

$$\sigma\ c(v_{h,p-1},\ m^n_{h,p-1}) + b(\boldsymbol{h}^n_{h,p},\ v_{h,p-1}) = (g,\ v_{h,p-1})_\Omega, \qquad \forall v_{h,p-1} \in \mathcal{S}_{h,k-1} \tag{19}$$

with $g = \tilde{f} - \sigma m^{n-1}_{h,p-1}$, where $\tilde{f}$ denotes an extrapolation of f at the previous time-step values of m_h that is determined by the specific type of the IMEX scheme, the remaining term in g is a contribution from temporal discretization of $\dot{m}_{h,p-1} = \sigma[m^n_{h,p-1} - m^{n-1}_{h,p}]$. Recall that for stability the orders used in Equations (18) and (19) for the flux and mass are p and $p-1$, respectively ($p > 1$). To simplify the notation, in the remainder of this section, the current unknowns $\boldsymbol{h}^n_{h,p}$ and $m^n_{h,p-1}$ are denoted as $\boldsymbol{h}_p$ and m_{p-1}.

5.1 | Residual and interface jump based error estimates

The *a posteriori* error estimate corresponding to the energy norm (17) of the error is derived from the following residual- and jump-based errors. Consider first a sufficiently refined regular mesh $\mathcal{T}_h$ of Ω, where h is the mesh parameter.

- Element residual errors corresponding to the constitutive and conservation of mass equations: let K be an element in $\mathcal{T}_h$, define

$$\eta_{K,R,1} := \|\boldsymbol{D}\nabla m_{p-1} - \boldsymbol{h}_p\|_{0,K}, \tag{20}$$

$$\eta_{K,R,2} := \|\sigma\ m_{p-1} + \mathrm{div}\boldsymbol{h}_p - g\|_{0,K}. \tag{21}$$

- Inter-element interface jump error: let e be an edge shared by two adjacent elements K^+ and K^-, then the jump error is defined by

$$\eta_{e,J} := h^{-1/2}\|[\![m_{p-1}]\!]\|_{0,e}, \tag{22}$$

where the jump operator is $[\![m_{p-1}]\!] = m^+_{p-1} - m^-_{p-1}$, m^+_{p-1}, and m^-_{p-1} are values of m_{p-1} at the edge e from the side of K^+ and K^-, respectively.

The local error estimate over a given element $K \in \mathcal{T}_h$ is thus defined by summing the error contributions from (20) to (22),

$$\eta_K := \left[\eta^2_{K,R,1} + \eta^2_{K,R,2} + \sum_{e\in\partial K}\eta^2_{e,J}\right]^{1/2}, \tag{23}$$

and the global error estimate is given by

$$\eta_{\mathcal{T}_h} := \left[\sum_{K\in\mathcal{T}_h}\left[\eta^2_{K,R,1} + \eta^2_{K,R,2}\right] + \sum_{e\in\Gamma_h}\eta^2_{e,J}\right]^{1/2}. \tag{24}$$

5.2 | Upper bound

The global residual error (24) provides an upper bound of the energy norm of the error. To show this, we make use of the following standard estimates

1. Optimality estimate: let $(\boldsymbol{h},\ m) \in H(\mathrm{div},\Omega)\times L^2(\Omega)$ be the exact solution at the current time-step, that is, t_n, then there exists $C > 0$, such that

$$\|\boldsymbol{h} - \boldsymbol{h}_p\|_{\mathrm{div},\Omega} + \|m - m_{p-1}\|_{0,\Omega} \le C\left\{\inf_{\boldsymbol{\tau}_p\in\mathcal{V}_p}\|\boldsymbol{h} - \boldsymbol{\tau}_p\|_{\mathrm{div},\Omega} + \inf_{v_{p-1}\in S_{p-1}}\|m - v_{p-1}\|_{0,\Omega}\right\}. \tag{25}$$

2. Energy norm error estimate of the finite element solution:

$$\begin{aligned}\|\boldsymbol{h}_p\|_{\mathrm{div},\Omega} + \|m_{p-1}\|_{0,\Omega} \le C\Bigg[&\sup_{\substack{\boldsymbol{\tau}_p\in\mathcal{V}_p\\ \|\boldsymbol{\tau}_p\|_{\mathrm{div},\Omega}=1}}\{a(\boldsymbol{\tau}_p,\ \boldsymbol{h}_p) - b(\boldsymbol{\tau}_p,\ m_{p-1})\}\\ &+ \sup_{\substack{v_{p-1}\in S_{p-1}\\ \|v_{p-1}\|_{0,\Omega}=1}}\{\sigma\ c(v_{p-1},\ m_{p-1}) + b(\boldsymbol{h}_p,\ v_{p-1})\}\Bigg],\end{aligned} \tag{26}$$

for some $C > 0$.

3. *Saturation assumption*: One of the most crucial ingredients towards the proof of an upper bound is the saturation assumption. Roughly, it states that the error norm decreases uniformly as we increase the order of approximation by one. More precisely, let $(\boldsymbol{h}_{p+1}, m_p)$ and $(\boldsymbol{h}_p, m_{p-1})$ be approximate solutions of (18) and (19), then there is $0 < \beta < 1$, such that

$$\|\boldsymbol{h} - \boldsymbol{h}_{p+1}\|_{\mathrm{div},\Omega} + \|m - m_p\|_{0,\Omega} < \beta\left[\|\boldsymbol{h} - \boldsymbol{h}_p\|_{\mathrm{div},\Omega} + \|m - m_{p-1}\|_{0,\Omega}\right]. \tag{27}$$

One can construct a mesh $\mathcal{T}_h$ on which such a saturation estimate does not hold, however, for sufficiently refined regular mesh it always hold true.

Having the above results for the upper bound, it is sufficient to show that the error between successive approximations is bounded from above. That is, there is a constant $C > 0$ such that

$$\|\boldsymbol{h}_{p+1} - \boldsymbol{h}_p\|_{\mathrm{div},\Omega} + \|m_p - m_{p-1}\|_{0,\Omega} \leq C\eta_{\mathcal{T}_h}. \tag{28}$$

To show this, since $(\boldsymbol{h}_p, m_{p-1})$ belongs to the test space $\mathcal{V}_{p+1} \times \mathcal{S}_p$, we note that

$$a(\boldsymbol{\tau}_{p+1},\ \boldsymbol{h}_{p+1} - \boldsymbol{h}_p) - b(\boldsymbol{\tau}_{p+1},\ m_p - m_{p-1}) = 0, \qquad \forall \boldsymbol{\tau}_{p+1} \in \mathcal{V}_{p+1} \tag{29}$$

$$\sigma\ c(v_p,\ m_p - m_{p-1}) + b(\boldsymbol{h}_{p+1} - \boldsymbol{h}_p,\ v_p) = 0, \qquad \forall v_p \in \mathcal{S}_p. \tag{30}$$

Hence, by the estimate (26), we have, for some $C > 0$,

$$\begin{aligned}
&\|\boldsymbol{h}_{p+1} - \boldsymbol{h}_p\|_{\mathrm{div},\Omega} + \|m_p - m_{p-1}\|_{0,\Omega} \\
&\leq C\Bigg[\sup_{\substack{\boldsymbol{\tau}_{p+1}\in\mathcal{V}_{p+1} \\ \|\boldsymbol{\tau}_{p+1}\|_{\mathrm{div},\Omega}=1}} \{a(\boldsymbol{\tau}_{p+1},\ \boldsymbol{h}_{p+1} - \boldsymbol{h}_p) - b(\boldsymbol{\tau}_{p+1},\ m_p - m_{p-1})\} \\
&+ \sup_{\substack{v_p\in\mathcal{S}_p \\ \|v_p\|_{0,\Omega}=1}} \{\sigma\ c(v_p,\ m_p - m_{p-1}) + b(\boldsymbol{h}_{p+1} - \boldsymbol{h}_p,\ v_p)\}\Bigg].
\end{aligned} \tag{31}$$

Now, since

$$a(\boldsymbol{\tau}_p,\ \boldsymbol{h}_{p+1} - \boldsymbol{h}_p) - b(\boldsymbol{\tau}_p,\ m_p - m_{p-1}) = 0, \quad \forall \boldsymbol{\tau}_p \in \mathcal{V}_p, \tag{32}$$

it follows for every $\boldsymbol{\tau}_p$ that

$$\begin{aligned}
&a(\boldsymbol{\tau}_{p+1},\ \boldsymbol{h}_{p+1} - \boldsymbol{h}_p) - b(\boldsymbol{\tau}_{p+1},\ m_p - m_{p-1}) \\
&= a(\boldsymbol{\tau}_{p+1} - \boldsymbol{\tau}_p,\ \boldsymbol{h}_{p+1} - \boldsymbol{h}_p) - b(\boldsymbol{\tau}_{p+1} - \boldsymbol{\tau}_p,\ m_p - m_{p-1}) \\
&= -a(\boldsymbol{\tau}_{p+1} - \boldsymbol{\tau}_p,\ \boldsymbol{h}_p) + b(\boldsymbol{\tau}_{p+1} - \boldsymbol{\tau}_p,\ m_{p-1}) \\
&= \sum_K \left\{(\boldsymbol{\tau}_{p+1} - \boldsymbol{\tau}_p,\ \boldsymbol{h}_p)_K + (\mathrm{div}(\boldsymbol{\tau}_{p+1} - \boldsymbol{\tau}_p),\ m_{p-1})_K\right\} \\
&= \sum_K \left\{-(\boldsymbol{\tau}_{p+1} - \boldsymbol{\tau}_p,\ \boldsymbol{h}_p)_K + (\boldsymbol{\tau}_{p+1} - \boldsymbol{\tau}_p,\ \nabla m_{p-1})_K\right\} + \sum_{e\in\Gamma_h} ([\boldsymbol{\tau}_{p+1} - \boldsymbol{\tau}_p]\cdot\boldsymbol{n},\ [\![m_{p-1}]\!])_e \\
&= \sum_K (\boldsymbol{\tau}_{p+1} - \boldsymbol{\tau}_p,\ \boldsymbol{h}_p - \nabla m_{p-1})_K + \sum_{e\in\Gamma_h} ([\boldsymbol{\tau}_{p+1} - \boldsymbol{\tau}_p]\cdot\boldsymbol{n},\ [\![m_{p-1}]\!])_e \\
&\leq \sum_K \|\boldsymbol{\tau}_{p+1} - \boldsymbol{\tau}_p\|_{0,K}\ \|\boldsymbol{h}_p - \nabla m_{p-1}\|_{0,K} + \sum_{e\in\Gamma_h} \|[\boldsymbol{\tau}_{p+1} - \boldsymbol{\tau}_p]\cdot\boldsymbol{n}\|_{0,e}\ \|[\![m_{p-1}]\!]\|_{0,e} \\
&= \sum_K \eta_{K,R,1}\|\boldsymbol{\tau}_{p+1} - \boldsymbol{\tau}_p\|_{0,K} + \sum_{e\in\Gamma_h} \eta_{e,J} h^{1/2} \|[\boldsymbol{\tau}_{p+1} - \boldsymbol{\tau}_p]\cdot\boldsymbol{n}\|_{0,e}.
\end{aligned}$$

Hence, we obtain that

$$\sup_{\substack{\boldsymbol{\tau}_{p+1}\in\mathcal{V}_{p+1} \\ \|\boldsymbol{\tau}_{p+1}\|_{\mathrm{div},\Omega}=1}} \{a(\boldsymbol{\tau}_{p+1},\ \boldsymbol{h}_{p+1} - \boldsymbol{h}_p) - b(\boldsymbol{\tau}_{p+1},\ m_p - m_{p-1})\} \leq C_1\{\sum_K \eta_{K,R,1}^2 + \sum_e \eta_{e,J}^2\ \}^{1/2}, \tag{33}$$

for some constant $C_1 > 0$. A similar argument also leads to

$$\sup_{\substack{v_p\in\mathcal{S}_p \\ \|\|_{0,\Omega}=1}} \{\sigma\ c(v_p,\ m_p - m_{p-1}) + b(\boldsymbol{h}_{p+1} - \boldsymbol{h}_p,\ v_p)\} \leq C_2\{\sum_K \eta_{K,R,2}^2\ \}^{1/2}. \tag{34}$$

Therefore, for $C = \max(C_1, C_2)$ we obtain the estimate (28). Employing the saturation estimate (27) and (28), it then follows that

$$\|\boldsymbol{h} - \boldsymbol{h}_p\|_{\mathrm{div},\Omega} + \|m - m_{p-1}\|_{0,\Omega} \leq \frac{C}{1-\beta}\eta_{\mathcal{T}_h}. \tag{35}$$

Here the constant C depends only on the approximation order p and h.

6 | ADAPTIVE p-REFINEMENT STRATEGY

Once the problem is solved with a given distribution of polynomial orders over the mesh entities, and the local *a posteriori* error η_K over each element $K \in \mathcal{T}_h$ is calculated, the next step is to apply a p-refinement strategy inspired by the well-known bulk-chasing Dörfler's criterion.[48] The refinement algorithm is characterized by two parameters $\theta_{\min}$ and $\theta_{\max}$, where $0 \leq \theta_{\min} < \theta_{\max} \leq 1$, and is performed in three stages:

Stage 1. Given *a posteriori* error estimate η_K on each element $K \in \mathcal{T}_h$ and $\eta_{MAX} = \max_{K\in\mathcal{T}_h}\{\eta_K\}$, the polynomial order over element K is raised by one if

$$\eta_K \geq \theta_{\max}\eta_{MAX},$$

or reduced by one if

$$\eta_K \leq \theta_{\min}\eta_{MAX}.$$

After applying this first stage of the adaptive process it may happen that the polynomial order distribution over adjacent elements is greater than one order. Numerical experiments (not presented here) revealed that such heterogeneity of polynomial order distribution results in undesirable oscillatory features in the approximated solution. Hence, following this step, certain smoothing of polynomial order over the mesh is required, which leads one to the next stage.

Algorithm 1. Pseudocode for the p-adaptive algorithm

```
Calculate η_K on each K ∈ T_h. Take θ_max and θ_min
[Stage 1. Setting order on each K]
for K ∈ T_h do
    if η_K ≥ θ_max η_MAX then
        raise polynomial order on K by one
    end if
    if η_K ≤ θ_min η_MAX then
        decrease polynomial order on K by one to not less than a minimum order chosen by the user, say 1
    end if
end for
[Stage 2. Order smoothing]
for E ∈ Γ_h shared by two elements K and K′ in T_h such that the order in K is greater than that of K′ by more than 1 do
    set: order in K′ equals order in K minus 1
end for
[Stage 3. Setting order on the interfaces]
for E ∈ Γ_h do
    if E is on the boundary with only one adjacent element K then
        set order on E to be equal to that of on K
    else
        find adjacent elements K and K′ sharing E
        Set: order on E to be maximum of orders on K and K′
    end if
end for
```

Stage 2. To smooth the polynomial order distribution, we force the difference in polynomial order between two adjacent elements K and K' to not exceed one, by resetting the order on the element with smaller degree to that of the higher degree minus one. That is, suppose $\text{order}(K) + 1 < \text{order}(K')$, then we reset $\text{order}(K) := \text{order}(K') - 1$.

Stage 3. This stage is responsible for maintaining the $H(\text{div})$-conformity of the space of flux functions after execution of the above two stages. For each interface entity E shared by two elements K and K', one sets the order as the maximum of the polynomial orders over K and K'.

The adaptive p-refinement algorithm consisting of the above three stages is summarized in Algorithm 1. Following the above p-adaptive stages, one also needs to adjust the quadrature rules over the mesh entities appropriately in order to match the polynomial order distributions optimally. Certain models of physical processes that are well described using diffusion-reaction equations introduce so-called internal variables (see Section 7.4 which considers a problem in electrophysiology).

The projection of field variables within an element upon change in the polynomial order is handled in a straightforward manner using the hierarchical finite element approach employed here. In addition, internal variables are treated here in the same spirit as field variables and approximated using an L^2 basis.

As is common with such schemes, the choice of the parameters $\theta_{\min}$ and $\theta_{\max}$ is informed by numerical experiment. This is an open research problem and therefore further work on such heuristic approaches is required.

7 | NUMERICAL EXAMPLES

Two groups of numerical examples are presented. The first compares the convergence of results of the mixed scheme and the standard single-field formulation in approximating important aspects of the solution. These include solutions involving singularities in Section 7.1, and computation of the speed of travelling wave solutions in Section 7.2. Suitability of the p-adaptive mixed formulation in terms of the features of the solution is also investigated. The second group, in Sections 7.3 and 7.4, showcases the capabilities of the p-adaptive, IMEX mixed formulation in simulating problems of practical importance, namely pattern formation and electrophysiology. We investigated various IMEX schemes, however, for the examples presented in this section we opted for the second-order additive Runge–Kutta scheme. This choice allows one to exploit the smoothness of the reaction terms using methods with high-order approximation in time, such as Runge–Kutta, thereby allowing larger time steps without sacrificing accuracy.

The computer implementation of the proposed numerical scheme is carried out using the open-source library MoFEM.[49] The library integrates and utilizes other open-source libraries such as MOAB, a mesh-oriented database,[50] and PETSc.[51] The MOAB library is used to store and manage mesh related data, while PETSc is used for parallel operations involving linear algebra.

The IMEX methods presented in Section 4 are implemented using the PETSc time solvers.[52]

7.1 | Convergence tests

Two cases are considered. In the first case, a spatially smooth solution is considered with a piece-wise temporal profile that stabilizes after some specified time. Thus, the approximation error after a sufficiently long simulation time is associated entirely with the spatial discretization. The second case considers the approximation of a one-species Fisher's type problem on a square domain Ω with heterogeneous diffusivity.

Smooth manufactured solution

It is well-known that both standard and mixed finite element formulations are optimal in terms of convergence in the L^2-norm, that is, $\mathcal{O}(h^{p+1})$, for sufficiently smooth solutions, where p is the order of the finite element space. Noting that the mesh size parameter h is inversely proportional to the number of DoF to the power dim, where $dim = 1, 2,$ or 3 is the space dimension, these optimality results are confirmed practically, as shown in Figure 2, by considering a manufactured solution based on the smooth function

$$g(x, y) = 1 + \sin(2\pi x)\sin(2\pi y), \qquad \text{for } (x, y) \in \Omega. \tag{36}$$

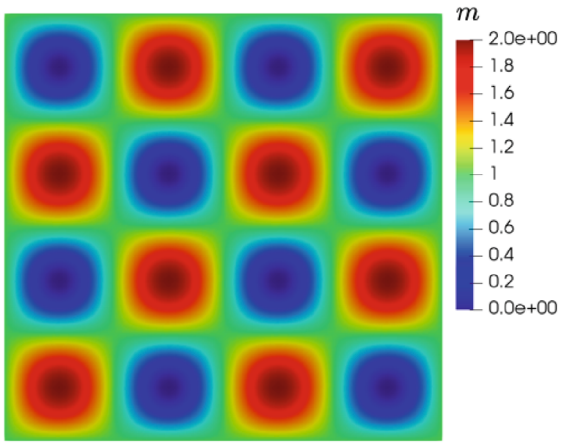

FIGURE 2 Exact (manufactured) solution for m at $t = 1$

Consider first a one-species diffusion-reaction system over the domain $\Omega = [-1, 1]^2$ (so that g vanishes on the boundary) with isotropic diffusivity $\boldsymbol{D} = d\boldsymbol{I}$, $d = 1$, and then assume the exact (manufactured) solution for the mass concentration m

$$m(x, y, t) = \begin{cases} t\, g(x, y), & t < t^*, \\ g(x, y), & t \geq t^*, \end{cases} \tag{37}$$

for some given t^*. The right-hand-side source term f is given by the residual of the exact solution, that is,

$$f := \dot{m} + \operatorname{div}(\boldsymbol{D}\nabla m).$$

Note that $\dot{m}$ and $\operatorname{div}(\boldsymbol{D}\nabla m)$ are also piecewise in time, that is,

$$\dot{m} = \begin{cases} g(x, y), & t < t^*, \\ 0, & t > t^*, \end{cases} \quad \text{and} \quad \operatorname{div}(\boldsymbol{D}\nabla m) = \begin{cases} t\, \operatorname{div}(\boldsymbol{D}\nabla g), & t < t^*, \\ \operatorname{div}(\boldsymbol{D}\nabla g), & t \geq t^*. \end{cases}$$

Consequently, the source term is also temporally piece-wise which stabilizes to a time-independent profile after t^*. Note also that for $t < t^*$, $\overline{m} = t$ on the boundary Γ, and for $t > t^*$, $\overline{m} = 1$. With this set up, the temporal discretization error after a time t sufficiently greater than t^* will be negligible, and the total error is dominated by the spatial approximation. In other words, it amounts to the approximation of the steady state case ($\dot{m} = 0$) with the manufactured solution $m = g$.

The convergence results presented in Figures 3 and 4 are obtained by a successive refinement of an initial uniform mesh with $h = 2/5$, and the inflection time t^* and a uniform time step length Δt are chosen to be 1 and 0.1, respectively, for each mesh. The simulations are run up to $t = 10$; a sufficiently long time to ensure that the temporal discretization error is negligible.

With the manufactured solution (37), the convergence rate of the mixed formulation with respect to the H^1-norm, given by

$$[\|m - m^h\|^2_{0,\Omega} + \|\boldsymbol{h} - \boldsymbol{h}^h\|^2_{0,\Omega}\,]^{1/2},$$

is expected to be one order higher than that of the standard formulation, as demonstrated in Figure 4. This is due to the fact that the flux $\boldsymbol{h}^h$ for the standard formulation is obtained by postprocessing from m^h, unlike the mixed formulation, wherein the flux is directly approximated as a primary field variable.

The next set of examples in this group aims at demonstrating the effectiveness of the p-adaptive mixed formulation in resolving fine features of solutions efficiently. For smooth solutions such as (36), the variability of the solution is almost uniform on the larger scale. In this case, the application of p-adaptivity is less effective since the error is distributed almost

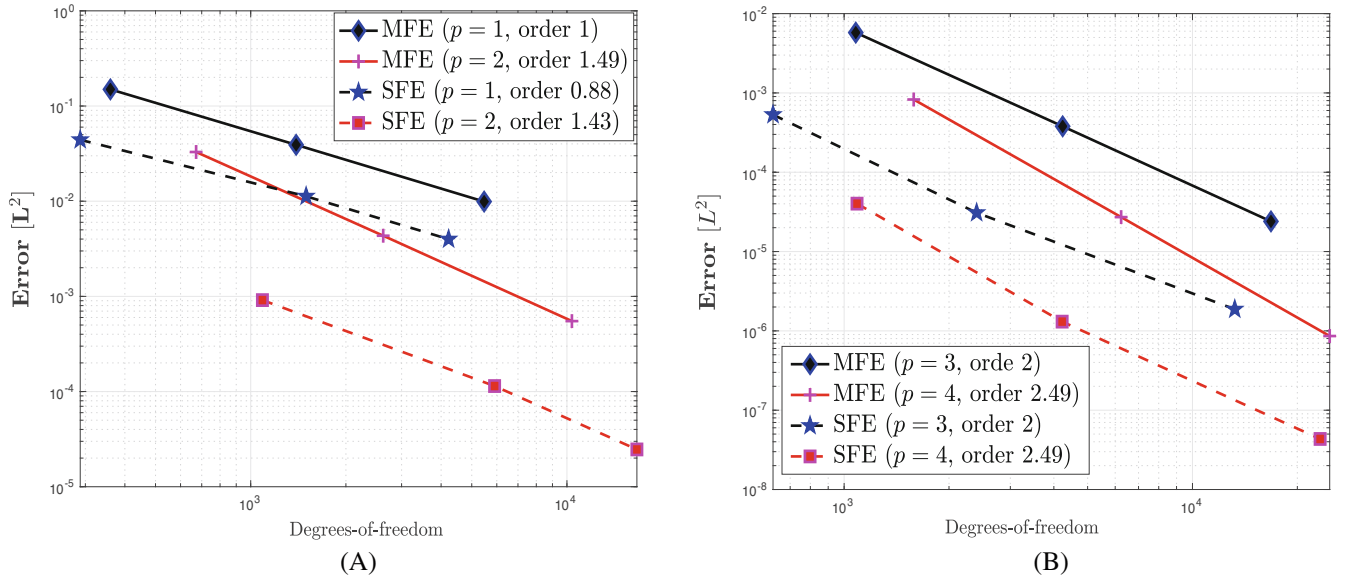

FIGURE 3 Comparison of convergence rates of the mixed (MFE) and standard (SFE) formulations with respect to the L^2 error norm. (A) For orders of approximation $p = 1, 2$, while (B) for $p = 3, 4$. The legend "order" stands for the absolute value of the slope of the convergence curve once a consistent slope is established between consecutive refinements

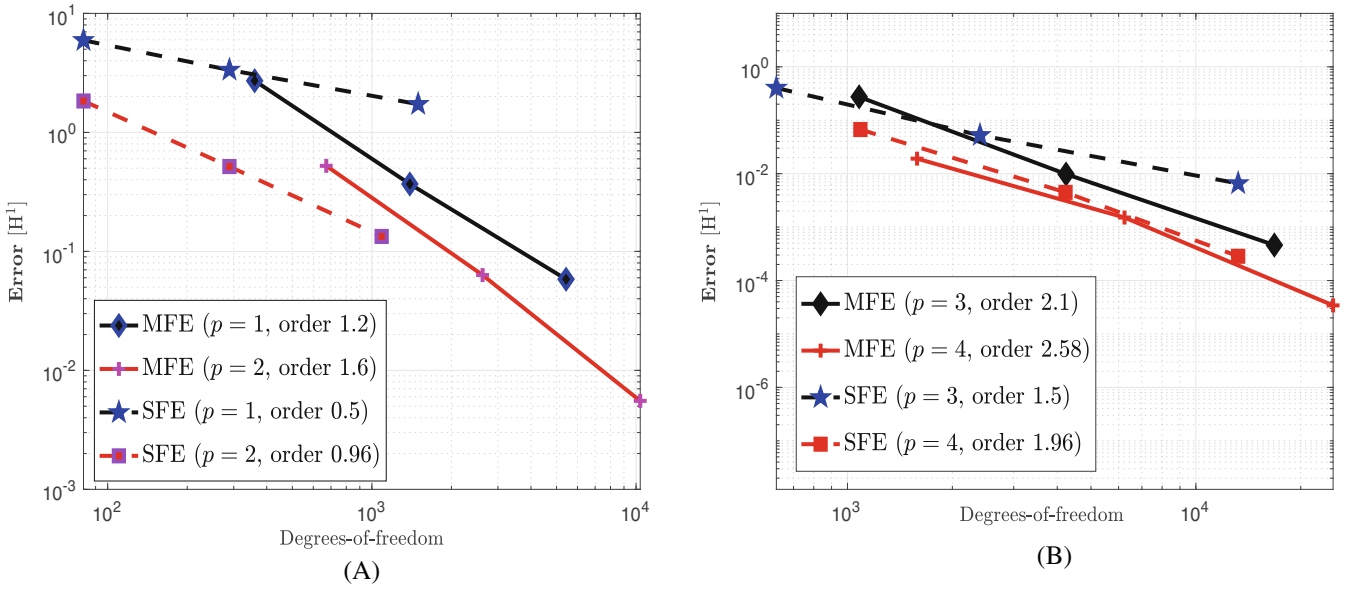

FIGURE 4 Comparison of convergence rate the mixed (MFE) and standard (SFE) formulations with respect to the H^1-norm. (A) For order of approximation $p = 1, 2$, for m while (B) for $p = 3, 4$. The legend "order" stands for the absolute value of the slope of the convergence curve once a consistent slope is established between consecutive refinements

uniformly. This is demonstrated in the convergence result displayed in Figure 5. It shows that the p-adaptive strategy with parameters $\theta_{\min} = 0.02$ and $\theta_{\max} = 0.8$, representing a quite conservative adaptive strategy, produces a convergence trend which is not generally better than that of the uniform p-refinement. As expected, at each adaptive step, as shown in Figure 6, the error is distributed almost uniformly, which leads to the marking of most of the elements for refinement. This corresponds to the convergence result shown in Figure 5, which is no better than the uniform p-adaptive strategy.

By contrast, when the solution is characterized by the presence of sudden spatial changes over the domain, such as travelling waves, the p-adaptive algorithm becomes most effective. To demonstrate this, we consider a smooth analytical

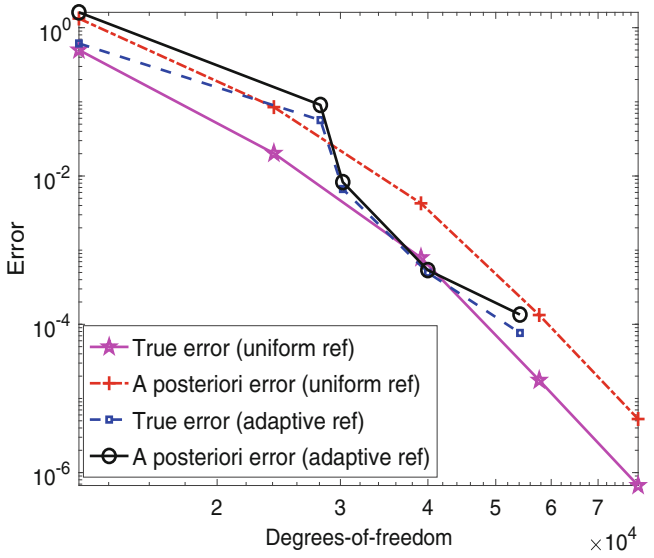

FIGURE 5 Comparison of the *p*-adaptive and uniform refinement strategies for smooth and slowly varying solution

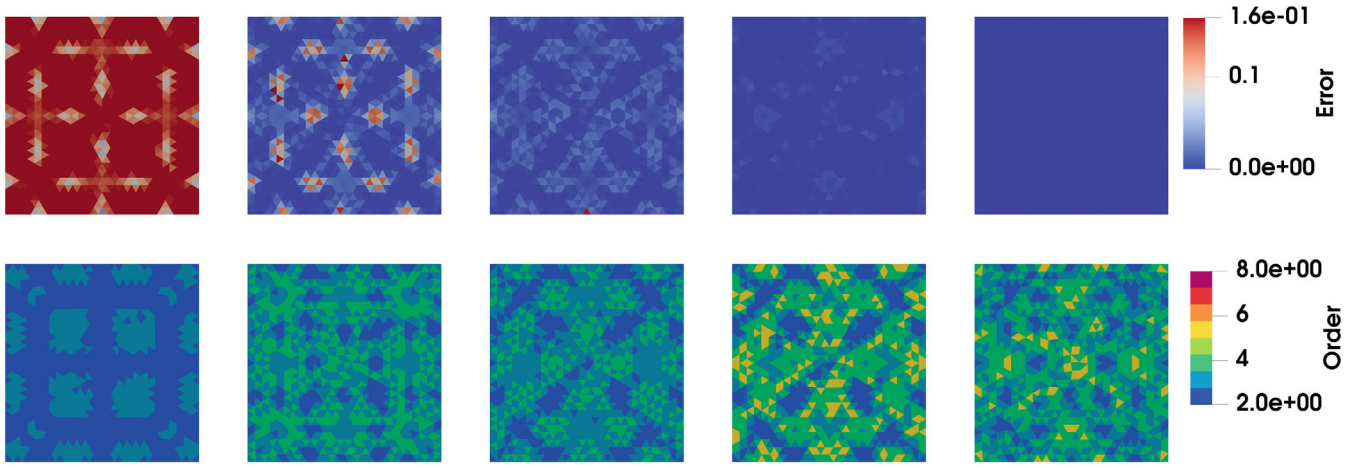

FIGURE 6 Distribution of error and polynomial order over the mesh at each *p*-adaptive iteration

solution (manufactured) replacing the g in Equation (36) by the bump function over the square domain $\Omega = [-1, 1]^2$,

$$g(x, y) = \begin{cases} \exp\left(\frac{-x^2-y^2}{r^2-x^2-y^2}\right) & \text{if } x^2 + y^2 < r^2, \\ 0 & \text{otherwise.} \end{cases} \tag{38}$$

where $r = 0.75$. As in the previous examples, the diffusion parameter is chosen such that $d = 1$, and $t^* = 1$ and $\Delta t = 0.1$. The error is computed at $t = 10$, as in the previous simulation, as it is far enough from the inflection time $t^* = 1$ so that the temporal discretization error becomes negligible. The spatial mesh is unstructured and relatively coarse. It can be easily seen that the bump function is infinitely many times differentiable, hence smooth. However, as can be seen from Figure 7, along the circle $x^2 + y^2 = r^2$ the solution changes drastically from zero to some finite non-zero value within a relatively small distance in the radial direction.

Thus it is expected that most of the error of the finite element approximation concentrates along the circle. This becomes evident in the distributions of the error as well as polynomial order over the mesh as displayed in the *p*-adaptive sequence as shown in Figure 9. The corresponding convergence result, shown in Figure 8, exhibits the better performance compared to the uniform *p*-adaptive strategy.

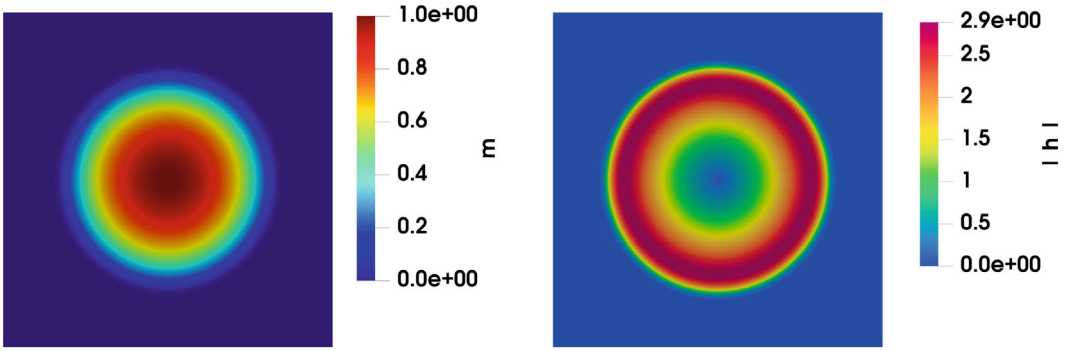

FIGURE 7 Bump function (left) and norm of the gradient (right)

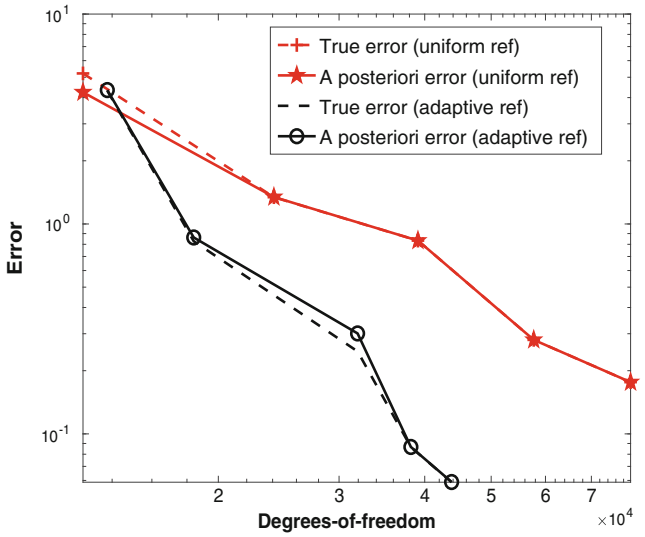

FIGURE 8 Convergence comparison between uniform and adaptive *p*-refinements for the bump function solution

Rough solution with singularities

Consider a one-species reaction diffusion problem on the square domain $\Omega = [-1,\ 1]^2$, with reaction kinetics of Fisher type,

$$f = m[1 - m]. \tag{39}$$

The domain is comprised of square patches with contrasting diffusivities $\boldsymbol{D} = d(\boldsymbol{x})\boldsymbol{I}$ with a checkerboard pattern, as shown in Figure 10 (A). For the blue patches $d = 0.1$ and for the remaining patches $d = 0.001$. An initial condition of $m^0 = 0.5$ on the center square and zero elsewhere is prescribed—see Figure 10 (B). A homogeneous flux boundary condition of the type given in Equation (4) is prescribed along the entire boundary Γ (i.e., $\overline{h} = 0$).

Solutions were computed up to $t = 6$ with a time-step size $\Delta t_n = 0.1$. Both the standard and mixed solutions were computed and compared. Because of the heterogeneous diffusivity, the solution develops kinks along the interfaces of the patches and singularities at the corners. It is important to note the well-known fact that such irregularities (singularities) cannot be resolved by increasing the polynomial order. A feasible way of resolving such features is using local *h*-adaptivity. In fact, numerical experimentation (not presented here) showed that *p*-adaptivity caused artificial oscillations near the corners as the polynomial order increases locally. For example, Figure 11 (B) shows the distribution of the flux magnitude, computed using the mixed method with the *a priori* adaptively refined mesh as shown in Figure 11 (A). Figures 11 (C) and 11 (D) show the mass distribution computed using the standard and mixed methods, respectively. Even though the reference mesh Figure 11 (A) has been used in both cases, the difference in their respective solutions is apparent. This

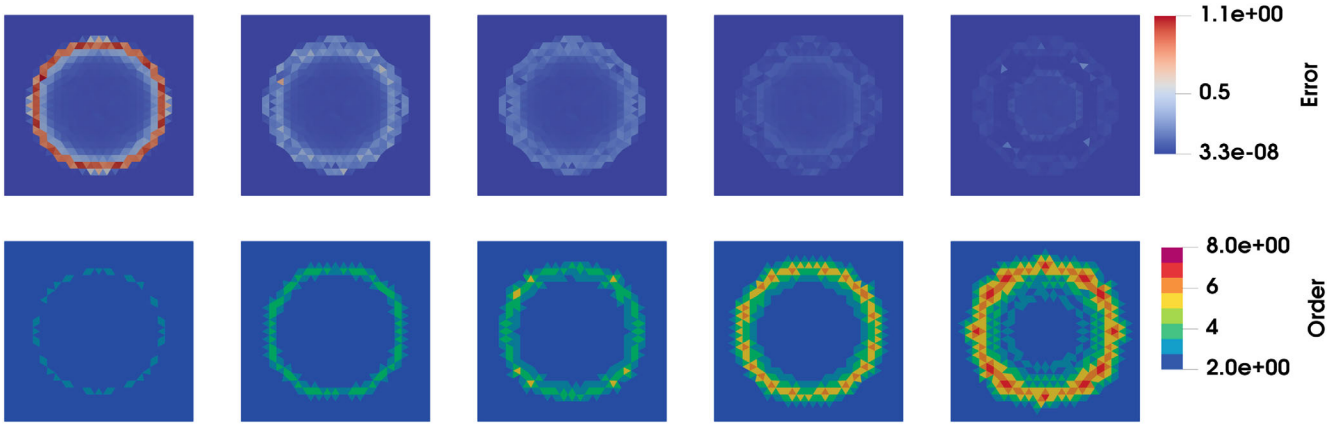

FIGURE 9 Distribution of the error (top row) and polynomial order (bottom row) in a *p*-adaptive sequence

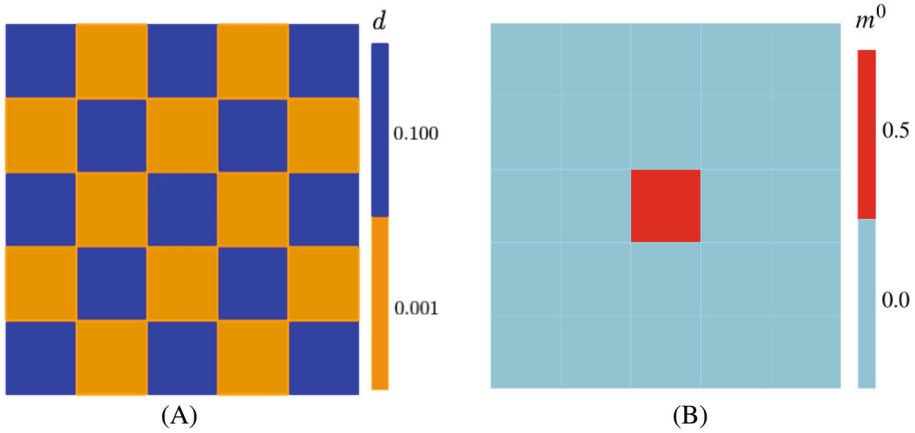

FIGURE 10 The heterogeneous domain $\Omega = [-1,\ 1]^2$ with a checkerboard pattern where in (A) the blue regions have $d = 1 \times 10^{-3}$ and the rest have $d = 1 \times 10^{-1}$, and in (B) an initial value $m^0 = 0.5$ is prescribed

is due to the fact that the standard formulation uses a H^1-conforming space and is unable to approximate solutions with features such as discontinuities and singularities. By contrast, the mixed formulation uses a non-conforming $L^2(\Omega)$ space for m^h and the exact, physically motivated conformity for the flux $\boldsymbol{h}^h$, that is, $H(\text{div})$. This allows the mixed method to capture such features.

Figure 12 shows the superiority of the mixed method over the standard single-field formulation. Here, the mass profiles along a line segment, colored in red in Figure 11 (A), that connects the center and the right top corner of the square domain Ω are displayed. Along this line segment, there are two interior corners of patches where discontinuities in m^h are expected. The solutions were obtained using various uniform meshes at different levels of refinement with parameter $h = 1/5, 1/10, 1/20$, and $1/40$, including a reference mesh (denoted by Ref. Mesh), which is obtained by refining along the interfaces and corners of the patches as in Figure 11 (A). The discontinuities at the interior corners are captured almost exactly using the mixed method regardless of the refinement level. By contrast, using the standard formulation, none of the meshes resulted in a reasonable approximation of the discontinuities. Another interesting observation is that the approximation of the mixed formulation converges from below. This is opposite to the standard formulation in which the approximation overestimates the solution.

7.2 | Speed of travelling wave solutions

The one-species Fisher-type Equation (39) supports travelling wave solutions. The wave nature of the solution depends on the relative size of the reaction and diffusion terms. When the reaction term is dominant, the wave front steepens and

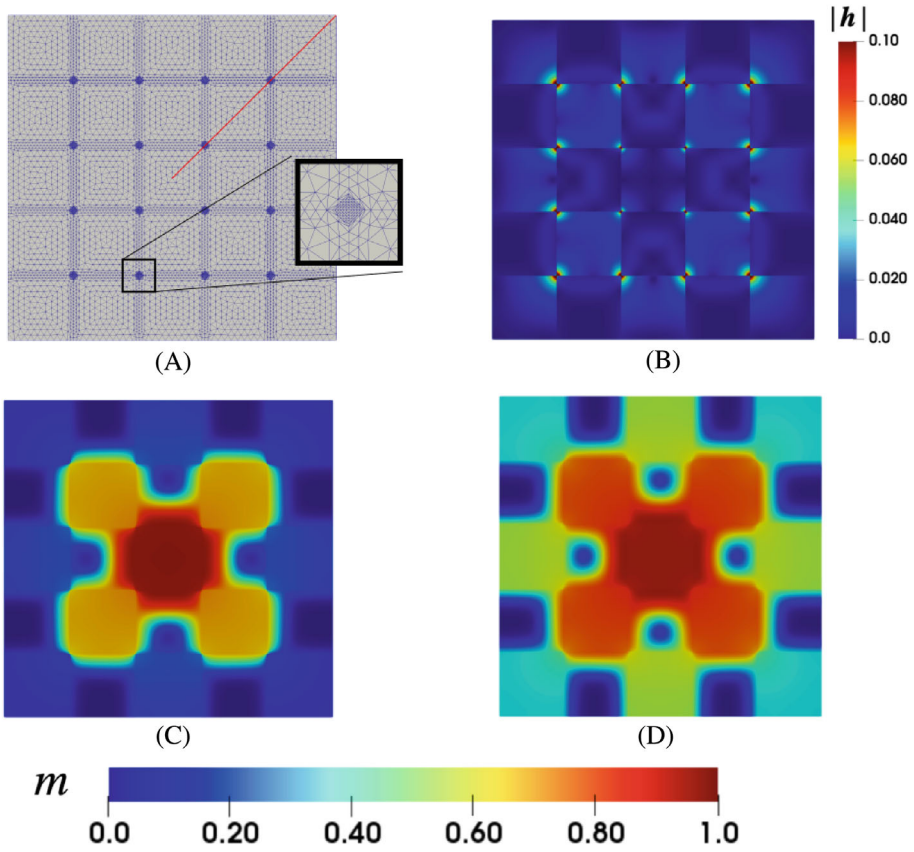

FIGURE 11 Comparison of approximations by standard and mixed methods, (A) an *a priori* adaptively refined mesh on which the mass concentration approximation at $t = 6$ are computed based on the standard (C) and mixed (D) methods. (B) Shows the distribution of the magnitude of flux, computed using the mixed method using the mesh (A) at $t = 6$, where singularities at the corners of the patches are shown

the wave travels with a finite speed. By contrast, when diffusion is dominant, the influence of the reaction term becomes less and the solution exhibits typical diffusion behavior, that is, it decays exponentially.

Consider the planar domain as shown in Figure 13, composed of rectangular patches that are arranged horizontally with increasing diffusivity between successive patches. The rectangular domain has height 0.8 and the width of the 5 patches are 0.6, 0.4, 0.4, 0.4, and 2.2. The maximum diffusivity $d = 0.5$ is chosen so that the problem remains in the wave propagation regime. As the initial condition, the mass concentration $m = 1$ is set on the first one-third of the left-most patch, while on the rest of the domain m is set to zero at $t = 0$. Since the diffusivity is smallest in the first left patch, the solution starts to evolve slowly with a sharp wave front. As the wave passes each interface, its speed increases while the sharpness of the wavefront decreases. The wavefront is identified using a levelset method based on a mass concentration value of 0.6. Uniform time steps of length $\Delta t = 0.05$ have been used. The position of the wavefront against time is presented in Figure 14 for various levels of mesh refinement. Importantly, the uniform approximations based on the mixed method are accurate and converge to the correct wave speed. However, the uniform approximation using the standard method initially overestimates the true speed of the travelling wave solution, and only slowly converges to the correct speed. The *p*-adaptive mixed formulation is used with the second coarsest mesh, and it is also obtained that the speed of the wave is in excellent agreement with that of the converged results of the mixed and standard methods.

7.3 | Pattern formation in ecological applications

The class of problems considered here have application in various important areas including biological pattern formation, morphogenesis[2] and electrophysiology.[53]

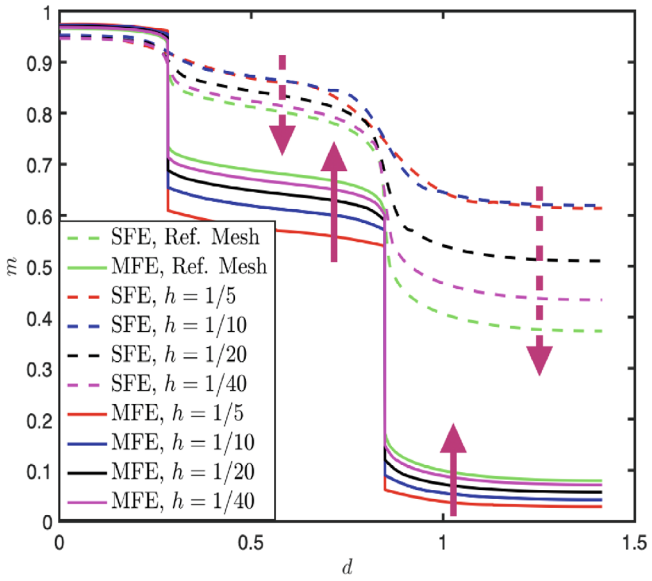

FIGURE 12 Mass concentration profile along a diagonal line from the center of the square to the right corner (as indicated in Figure 11 (A) with a red line segment) at $t = 6$. Various uniform meshes at different refinement levels described by the mesh parameter h along with a reference mesh (designated as Ref. Mesh), which was adaptively refined along the interfaces and corners of the patches, were used

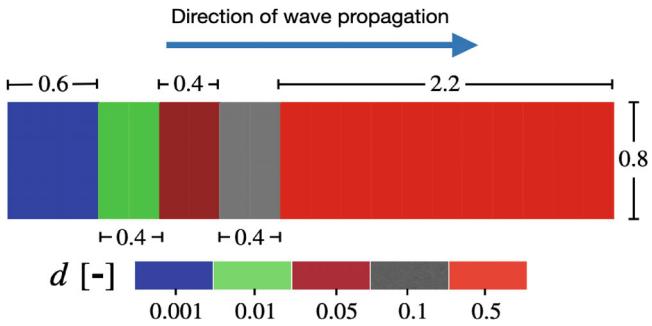

FIGURE 13 Domain for the travelling wave problem. Color indicates the diffusivity, which is piecewise constant and increasing towards the right

Segregation pattern

A competition-diffusion model involving three interacting species is considered. The level and mode of interaction between the species is the same. This, in effect, means that the magnitude of each species that is consumed by the others is the same as the other species that consumes it. The reaction term, for each $i = 1, 2, 3$, is given by

$$f_i = m_i[1 - a_{i1}m_1 - a_{i2}m_2 - a_{i3}m_3], \tag{40}$$

where the parameters in the model are represented in Table 1. It is assumed that all the three species have the same mobility rates, that is, $\boldsymbol{D} = d\boldsymbol{I}$, where $d = 0.01$. In cases where the dynamics is largely influenced by the reaction term, it is important to analyze the local stability of the spatially homogeneous problem (i.e., ignoring the diffusion terms). Such an analysis provides important insights into the range of parameter values for various possible spatio-temporal interaction patterns. A local stability analysis of the problem described by Equation (40) reveals eight equilibrium points of which only, $[m_1,\ m_2,\ m_3]_1 = [1/a_{11},\ 0,\ 0]$, and $[m_1,\ m_2,\ m_3]_2 = [0,\ 1/a_{22},\ 0]$, and $[m_1,\ m_2,\ m_3]_3 = [0,\ 0,\ 1/a_{33}]$ are quasi-stable. In the case of the segregation problem, these equilibrium points represent regions which are exclusively occupied by one of the species.

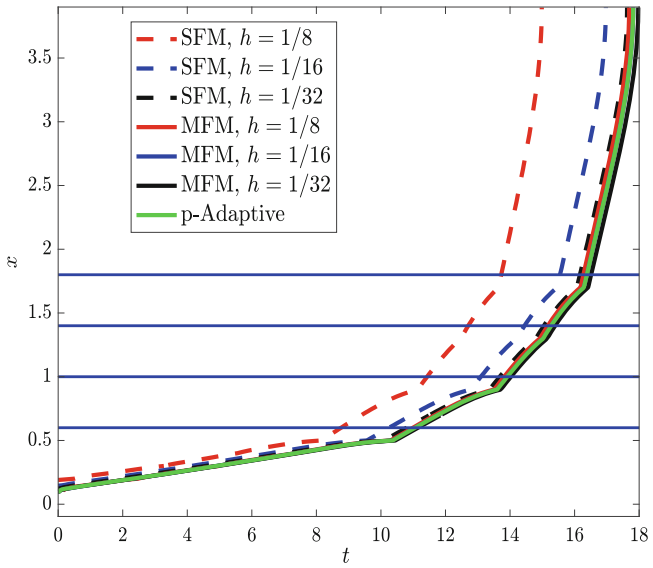

FIGURE 14 Comparison of speed of travelling wave solution with time. The broken lines correspond to the computation using the standard formulation (SFM) while the solid lines correspond to the mixed formulation (MFM). The horizontal lines mark the interface positions in the solution domain

TABLE 1 List of parameters for three species segregation problem

d_1	d_2	d_3	a_{11}	a_{12}	a_{13}	a_{21}	a_{22}	a_{23}	a_{31}	a_{32}	a_{33}
0.01	0.01	0.01	1	3	3	3	1	3	3	3	1

It is assumed initially that all three species are distributed randomly over the domain $\Omega = [-1,\ 1]^2$ as shown in Figure 15. Such problems have been studied previously.[19,54] In those studies the numerical approaches were either the finite difference method or the standard FEM.

A relatively coarse mesh for such a problem is used, but to sufficiently represent the random initial condition and to capture the fast dynamics at the beginning stage, order-6 polynomial approximation are used as shown in the lower left corner of Figure 15. During the early stages of evolution, as show in Figure 15 at $t = 0$ through $t = 10$, the dynamics appears to be reasonably fast. Eventually, as shown in the second row of Figure 15, as the species start to establish themselves into well defined regions each occupied by one of the species, the interaction starts to proceed in a slower manner. During this time the error distribution becomes more concentrated in the vicinity of the boundaries of these regions. It is shown that the polynomial adaptation follows the error distribution very closely. These regions tend to a quasi-stable configuration, that is patches of convex shapes with triple junctions with angle of separation given by $2\pi/3$.

Cyclic interaction

Here a three-species competition-diffusion system of equations with the reaction term given by Equation (40) is considered. The species react with each other in a cyclic way (based on parameters in Table 2) resulting in various complex spatio-temporal patterns such as spiral-like, and band-like structures depending on the topology of the habitat and the initial configuration.

A square habitat $\Omega = [-1,\ 1]^2$ is considered with initial configuration as shown in Figure 16 at $t = 0$ (top row left). The parameter values considered in the simulations are presented in Table 2. A relatively coarse mesh is used for such problem whose solution have complex, fine and spiral structure. A uniform time stepping is also used with step size $\Delta t = 0.2$. Initially the polynomial order is set to 2 and adaptively increases to 6 (with parameter $\theta_{\max} = 0.6$ and $\theta_{\min} = 0.1$) throughout the simulation. As shown in Figure 16, a spiral pattern starts to form turning in a clockwise direction. The spiral shape consists of stripes of each species lying side-by-side, and eventually fills the region and continues with the

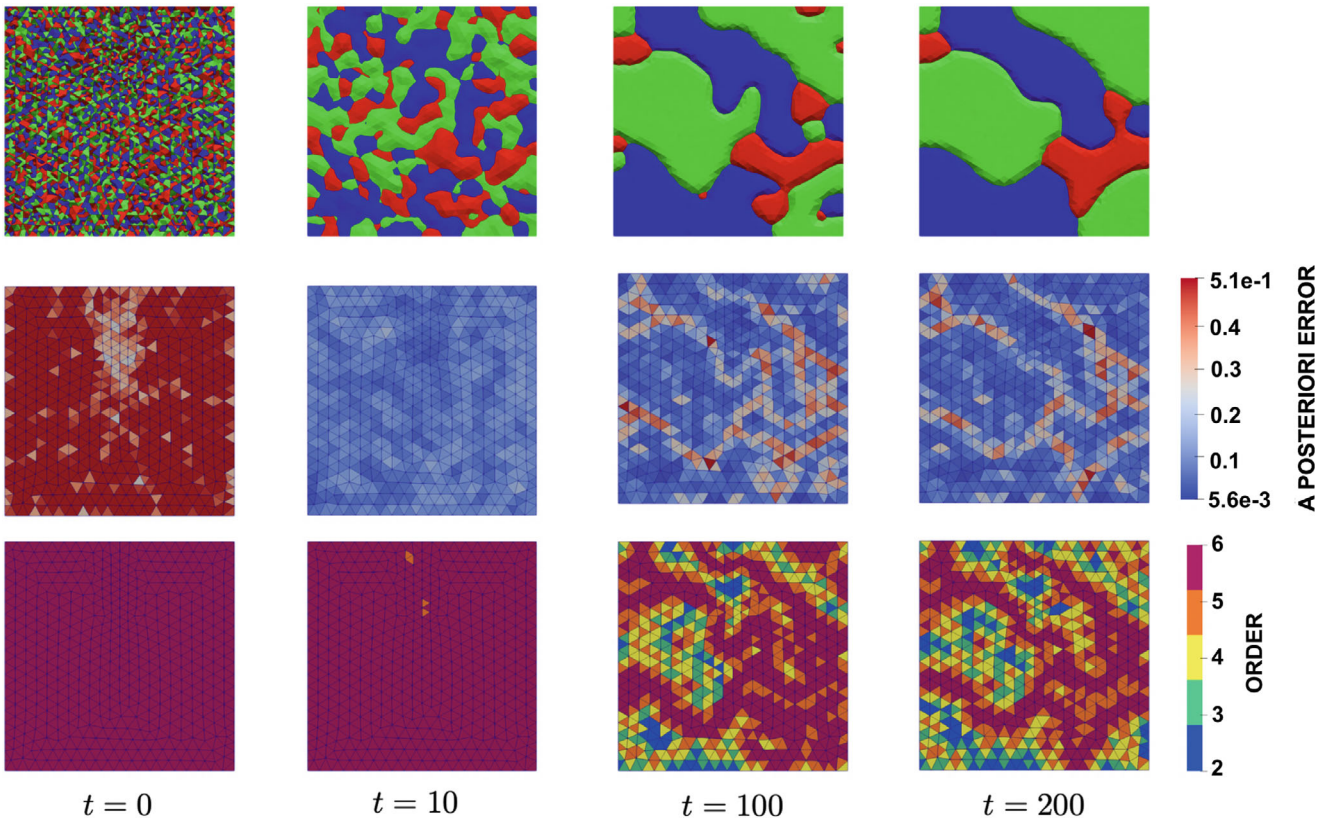

FIGURE 15 Development of segregation pattern as a result of interactions of the three species (Equation 40, Table 1) at various times. The blue color surface plot represents the region dominated by m_1 (i.e., $m_1 > m_2$ and $m_1 > m_3$), the red color surface plot by m_2, and the green surface plot by m_3

TABLE 2 List of parameters for three species cyclic interaction problem

d_1	d_2	d_3	a_{11}	a_{12}	a_{13}	a_{21}	a_{22}	a_{23}	a_{31}	a_{32}	a_{33}
0.01	0.01	0.01	1	2	7	7	1	2	2	7	1

same spiral feature. It is also shown that the error is high in the vicinity of the interface between the species which led to the adaptivity taking place only on elements around such interfaces. This clearly shows the efficiency of the *p*-adaptive mixed method.

7.4 | Spiral wave re-entry in electrophysiology

The propagation of ionic current in the cardiac muscle can be simulated using a mono-domain model, which is mathematically equivalent to the diffusion-reaction equation. The transmembrane electric potential can be viewed as a diffusing species, which "reacts" locally with the cellular ion channel densities. The reaction term depends on the ion channel densities through a set of highly nonlinear and coupled ordinary differential equations. Thus, the ion channel densities can be viewed as non-diffusing species and treated simply as internal state variables. There are a large number of models available for the reaction term (called cardiac electrophysiology models) with varying degrees of complexity in terms of the number of (internal) variables. Using the proposed mixed method, we simulate the phenomenon of spiral wave re-entry—the cause of several cardiac arrhythmias, such as ventricular tachycardia, atrial flutter, and atrial and ventricular fibrillation.

A square block of cardiac tissue of dimension 100 mm is considered. The domain is subdivided into a relatively coarse triangular mesh. The propagation of the transmembrane electric potential (more commonly known as the action potential) is governed by

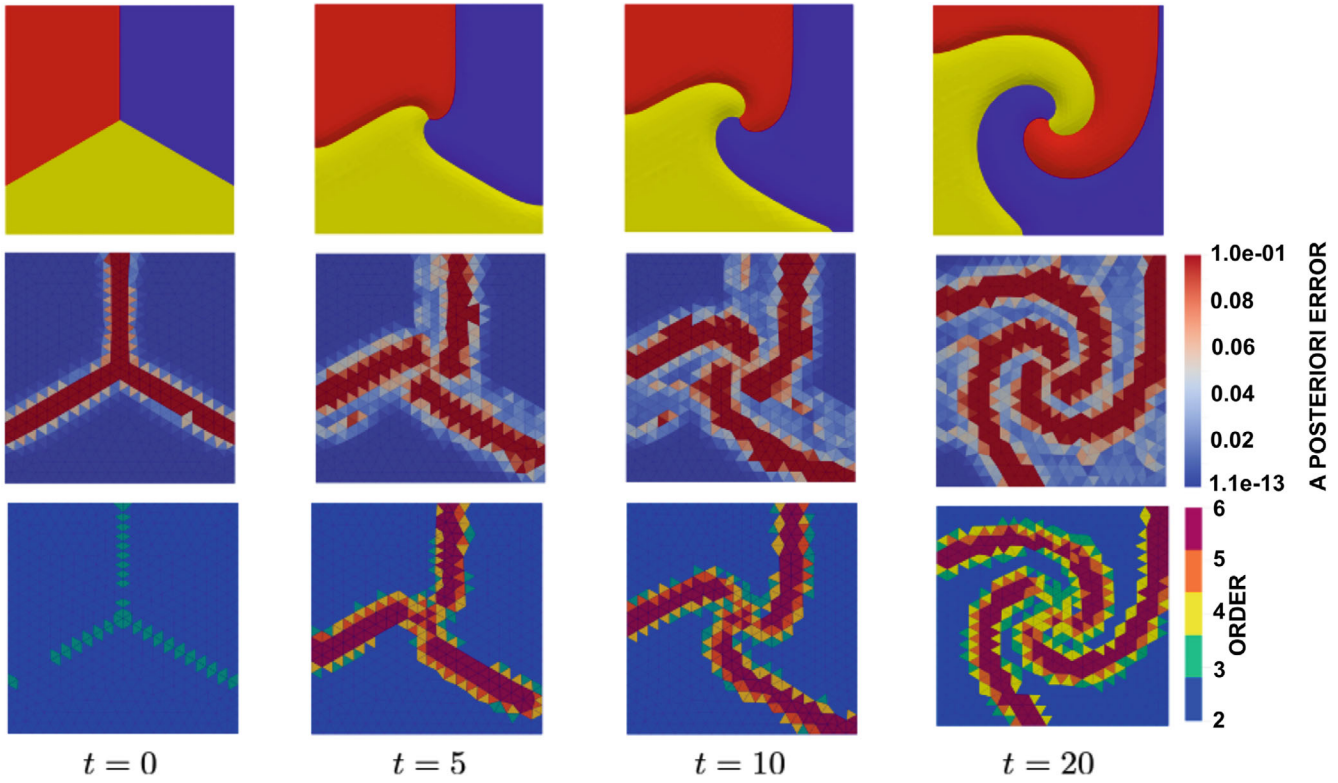

FIGURE 16 Development of spiral pattern as a result of cyclic interactions of three species (Equation 40, Table 2) at various stages. Region with blue depicts m_1, red m_2, and yellow m_3

$$\frac{\mathrm{d}}{\mathrm{d}\tau}m - \mathrm{div}(\boldsymbol{D}\nabla m) = f(m, r) + I_{\Omega'}(\tau), \tag{41}$$

where the non-dimensional variable $m \in [0, 1]$ is related to the transmembrane action potential E (mV) through the relation

$$E = [100m - 80] \text{ mV},$$

r is a single internal variable representing the density of ionic channels, and $I_{\Omega'}$ is the external stimulus. The time t (ms) is non-dimensionalized as

$$t = 12.9\ \tau \text{ ms}.$$

One of the simplest models capable of reproducing the spiral wave re-entry, the Aliev-Panfilov model,[9] is adopted for the reaction term:

$$f(m, r) = cm[m - \alpha][1 - m] - rm. \tag{42}$$

Equation (42) is supplemented by an ordinary differential equation for the recovery (internal state) variables r:

$$\frac{\mathrm{d}}{\mathrm{d}\tau}r = \left[\gamma + \frac{\mu_1 r}{\mu_2 + m}\right][-r - cm[m - b - 1]], \tag{43}$$

where the parameters appearing in Equations (42) and (43) are given in Table 3. We assume the conductivity to be isotropic, that is, $\boldsymbol{D} = d\boldsymbol{I}$. The time integration of Equation (43) together with the reaction term of Equation (41) are

TABLE 3 List of parameters for spiral wave re-entry problem

d (mm^2)	α	γ	b	c	μ	μ_2
0.01	0.01	0.01	1	2	7	7

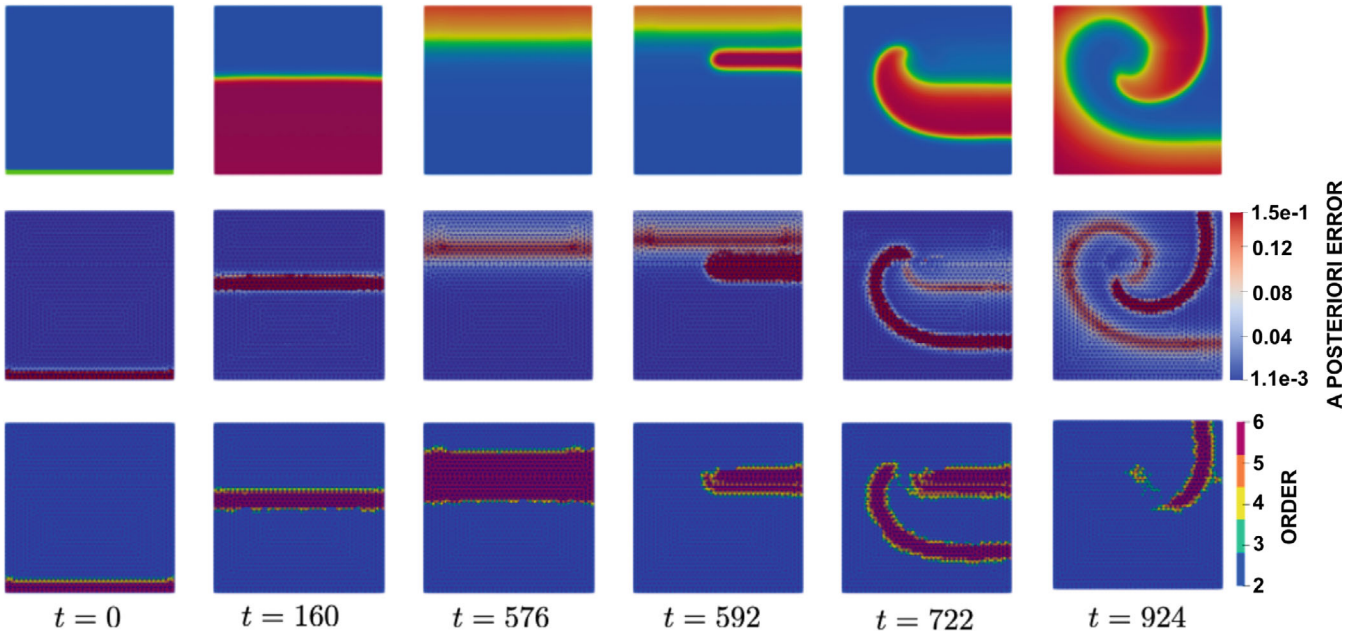

FIGURE 17 Evolution of a planar wave into a rotating spiral wave re-entry as a result of external stimulation $I_{\Omega'} = 40$ applied on a section of the domain during the time interval $t = 565$ ms to $t = 575$ ms. The planar wave is initiated with an initial excitation of $E(t = 0) = -40$ mV

carried out using the explicit part of the IMEX method. The p-adaptivity strategy with parameters $\theta_{\max} = 0.7$ and $\theta_{\min} = 0.03$ starts uniformly with order $p = 2$ and increases locally to order $p = 6$.

A horizontal planar wave is initiated by setting the action potential to $E = -40$ mV on the region between $y = 0$ and $y = 3$. The wave form continues to propagate upwards as seen from the snapshot at $t = 160$ ms.

Before the depolarizing tail disappears, an external stimulus $I_{\Omega'}$ is applied to the strip of region, defined by $\Omega' = \{(x, y) : 50 < x < 100,\ 67 < y < 70\}$, in order to initiate the spiral wave re-entry. The stimulus has magnitude 40 and is applied at $t = 565$ ms for a duration of 10 ms. This results in the development of the wavebreak (shown in Figure 17 at $t = 772$ ms). The wavebreak then evolves into a stable rotating vortex, as shown in the snapshots at $t = 924$ ms, and continues afterwards. The computational aspects of this problem have been considered by several researchers in the electrophysiology and electromechanics community. One notable work is by Göktepe and Kuhl[53] in which they used the standard finite element approach with an implicit time integration scheme on a structured quad mesh. The proposed p-adaptive, IMEX mixed method, as compared to their work, is seen to capture the spiral wave re-entry dynamics more efficiently.

8 | CONCLUSION

A family of p-adaptive IMEX, mixed finite element formulations has been proposed for a general class of diffusion-reaction based problems. In contrast to single-field, standard finite element formulations, this class of methods provides accurate approximations of a wider class of solutions, including those with less regularity. A standard formulation was shown to converge poorly, if at all, for such problems. The IMEX approach has been shown to be efficient and eliminates the dependence of algorithmic stability on the size of the spatial mesh size by handling the non-local diffusion part implicitly. This advantageous feature allows for mesh refinement, for example in an adaptive strategy, without the need for

changing the time step size Δt. The explicit treatment of the local reaction term makes the implementation generic and modular for various classes of reaction kinetics as demonstrated by the wide range of problems that have been analyzed here. The finite element spaces are built using a hierarchical construction which, in addition to offering optimal conditioning of the resulting linear system, makes the use of the *p*-adaptivity strategy a natural choice.[44] The mixed formulation introduces additional DoF. However, the computational complexity due to this increase in DoF can be handled efficiently using static condensation as the mass concentration field (which is in L^2) can be inverted locally since the local contributions are decoupled from one another. Moreover, this local inversion can also be used in block iterative schemes that involves computation of the Schur complement as an intermediate step. The Schur complement can then be computed exactly, resulting in a sparse global structure, rather than reverting to the common practice of approximating it.

A distinguishing feature of the mixed formulation is that it leads to straightforward derivation and implementation of residual-based a posteriori error estimations without the need for computationally demanding postprocessing effort as is usually the case in literature, see, for example.[43,55,56] This feature together with the hierarchical approximation of the mixed FEM is exploited in formulating the *p*-adaptive strategy. It has been demonstrated by a range of examples that the *p*-adaptive algorithm performs extremely well in efficiently resolving fine features.

The performance of the proposed formulation is demonstrated by a number of challenging examples. The advantages of the proposed method over the standard techniques are showcased by a problem that has singularities (see Section 7.1); and another one that supports travelling wave solutions (see Section 7.2). The capability of this general *p*-adaptive framework is demonstrated by applying it to problems arising from different applications such as electrophysiology, and spatial pattern formation in theoretical ecology.[4,54,57]

The *a posteriori* error indicator proposed is well-suited for local *p*-adaptivity. The results presented suggest that the approach is reliable. However, rigorous analysis should be undertaken to determine the tightness of the bounds in the estimate and thereby assess its reliability.

Through a straightforward generalization the proposed mixed method can be coupled to the mechanical deformation field for applications in cardiac electromechanics and chemo-mechanics. Due to the explicit treatment of the reaction term, the approach can be easily linked with, for example, electrophysiology models in the CellML repository.[56] Similarly, due to this explicit treatment of the reaction term, our computational approach can be easily used to drive the form of reaction kinetics models from experimental data following the approach proposed in Brunton et al.[58]

ACKNOWLEDGMENT

The authors gratefully acknowledge the support provided by the EPSRC Strategic Support Package: Engineering of Active Materials by Multiscale/Multiphysics Computational Mechanics—EP/R008531/1.

ORCID

Mebratu F. Wakeni https://orcid.org/0000-0002-1995-0853
Łukasz Kaczmarczyk https://orcid.org/0000-0002-8468-5435
Ignatios Athanasiadis https://orcid.org/0000-0003-2589-9131

REFERENCES

1. Chaplain MAJ, Ganesh M, Graham IG. Spatio-temporal pattern formation on spherical surfaces: numerical simulation and application to solid tumour growth. *J Math Biol*. 2001;42(5):387-423.
2. Garikipati K. Perspectives on the mathematics of biological patterning and morphogenesis. *J Mech Phys Solids*. 2017;99:192-210.
3. Ambrosi D, Ateshian GA, Arruda EM, et al. Perspectives on biological growth and remodeling. *J Mech Phys Solids*. 2011;59(4):863-883.
4. Morishita Y, Iwasa Y. Growth based morphogenesis of vertebrate limb bud. *Bull Math Biol*. 2008;70(7):1957-1978.
5. Tewary M, Ostblom J, Prochazka L, et al. A stepwise model of reaction-diffusion and positional information governs self-organized human peri-gastrulation-like patterning. *Development*. 2017;144(23):4298-4312.
6. Sebastian AM, Adrian M. A two-scale reaction–diffusion system with micro-cell reaction concentrated on a free boundary. *Comptes Rendus Mécanique*. 2008;336(6):481-486.
7. Ryser MD, Komarova SV, Nigam N. The cellular dynamics of bone remodeling: a mathematical model. *SIAM J Appl Math*. 2010;70(6):1899-1921.
8. Kerckhoffs RCP, Healy SN, Usyk TP, McCulloch AD. Computational methods for cardiac electromechanics. *Proc IEEE*. 2006;94(4):769-783.
9. Aliev RR, Alexander P. A simple two-variable model of cardiac excitation. *Chaos Solitons Fract*. 1996;7(3):293-301.
10. Zhang Y, Zhao XQ. A reaction-diffusion Lyme disease model with seasonality. *SIAM J Appl Math*. 2013;73(6):2077-2099.

11. Hemami M, Parand K, Rad JA. Numerical simulation of reaction-diffusion neural dynamics models and their synchronization/desynchronization: application to epileptic seizures. *Comput Math Appl*. 2019;78(11):3644-3677.
12. Olmos D, Shizgal BD. Pseudospectral method of solution of the Fitzhugh-Nagumo equation. *Math Comput Simul*. 2009;79(7):2258-2278.
13. Ramos JI. A review of some numerical methods for reaction-diffusion equations. *Math Comput Simul*. 1983;25(6):538-548.
14. Barkley DA. A model for fast computer simulation of waves in excitable media. *Phys D Nonlinear Phenomena*. 1991;49(1):61-70.
15. Ruiz-Baier R. Primal-mixed formulations for reaction-diffusion systems on deforming domains. *J Comput Phys*. 2015;299:320-338.
16. Tuncer N, Madzvamuse A, Meir AJ. Projected finite elements for reaction-diffusion systems on stationary closed surfaces. *Appl Numer Math*. 2015;96:45-71.
17. MacDonald G, Mackenzie JA, Nolan M, Insall RH. A computational method for the coupled solution of reaction-diffusion equations on evolving domains and manifolds: application to a model of cell migration and chemotaxis. *J Comput Phys*. 2016;309:207-226.
18. Landsberg C, Voigt A. A multigrid finite element method for reaction-diffusion systems on surfaces. *Comput Visual Sci*. 2010;13:177-185.
19. Mergia WD, Patidar KC. High-order semi-implicit linear multistep LG scheme for a three species competition-diffusion system in two-dimensional spatial domain arising in ecology. *Commun Nonlinear Sci Numer Simul*. 2020;84:1-16.
20. Mackenzie J, Rowlatt C, Insall R. A conservative finite element ALE scheme for mass-conservative reaction-diffusion equations on evolving two-dimensional domains. *SIAM J Sci Comput*. 2021;43(1):B132-B166.
21. Boffi D, Brezzi F, Fortin M, eds. *Mixed Finite Element Methods and Applications*. Springer Series in Computational Mathematics. Vol 44. Springer; 2013.
22. Franca LP, Hughes Thomas JR. Two classes of mixed finite element methods. *Comput Methods Appl Mech Eng*. 1988;69(1):89-129.
23. Arnold DN. Mixed finite element methods for elliptic problems. *Comput Methods Appl Mech Eng*. 1990;82(1):281-300.
24. Fu H, Guo H, Hou J, Zhao J. A stabilized mixed finite element method for steady and unsteady reaction-diffusion equations. *Comput Methods Appl Mech Eng*. 2016;304:102-117.
25. Liu Y, Feng Y, Zhang R. A high order conservative flux optimization finite element method for steady convection-diffusion equations. *J Comput Phys*. 2021;425:109895.
26. Kadeethum T, Lee S, Ballarin F, Choo J, Nick HM. A locally conservative mixed finite element framework for coupled hydro-mechanical-chemical processes in heterogeneous porous media. *Comput Geosci*. 2021;512:104774.
27. Kim K-Y. Guaranteed and asymptotically exact a posteriori error estimator for lowest-order Raviart-Thomas mixed finite element method. *Appl Numer Math*. 2021;165:357-375.
28. Jin M, Feng X, Wang K. Gradient recovery-based adaptive stabilized mixed FEM for the convection-diffusion-reaction equation on surfaces. *Comput Methods Appl Mech Eng*. 2021;380:113798.
29. Hu J, Yu G. A unified analysis of quasi-optimal convergence for adaptive mixed finite element methods. *SIAM J Numer Anal*. 2018;56(1):296-316.
30. Li Y. Some convergence and optimality results of adaptive mixed methods in finite element exterior calculus. *SIAM J Numer Anal*. 2019;57(4):2019-2042.
31. Barrenechea GR, Poza AH, Yorston H. A stabilised finite element method for the convection-diffusion-reaction equation in mixed form. *Comput Methods Appl Mech Eng*. 2018;339:389-415.
32. Bériot H, Prinn A, Gabard G. Efficient implementation of high-order finite elements for Helmholtz problems. *Int J Numer Methods Eng*. 2016;106:213-240.
33. Chaudhry JH, Estep D, Ginting V, Shadid JN, Tavener S. A posteriori error analysis of IMEX multi-step time integration methods for advection-diffusion-reaction equations. *Comput Methods Appl Mech Eng*. 2015;285:730-751.
34. Chalmers N, Agbaglah G, Chrust M, Mavriplis C. A parallel hp-adaptive high order discontinuous Galerkin method for the incompressible Navier-Stokes equations. *J Comput Phys X*. 2019;2:100023.
35. Ainsworth M, Ma X. Non-uniform order mixed FEM approximation: implementation, post-processing, computable error bound and adaptivity. *J Comput Phys*. 2012;231(2):436-453.
36. Ern A, Vohralík M. Polynomial-degree-robust a posteriori estimates in a unified setting for conforming, nonconforming, discontinuous Galerkin, and mixed discretizations. *SIAM J Numer Anal*. 2015;53(2):1058-1081.
37. Ascher UM, Ruuth SJ, Wetton BT. Implicit-explicit methods for time-dependent partial differential equations. *SIAM J Numer Anal*. 1995;32(3):797-823.
38. Singh S, Bansal D, Kaur G, Sircar S. Implicit-explicit-compact methods for advection diffusion reaction equations. *Comput Fluids*. 2020;212:104709.
39. Wang H, Shu C-W, Zhang Q. Stability and error estimates of local discontinuous Galerkin Methods with implicit-explicit time-marching for advection diffusion problems. *SIAM J Numer Anal*. 2015;53(1):206-227.
40. Bürger R, Gavilán E, Inzunza D, Mulet P, Villada LM. Implicit-explicit methods for a convection-diffusion-reaction model of the propagation of forest fires. *Mathematics*. 2020;8:1034.
41. Meng F, Banks JW, Henshaw WD, Schwendeman DW. Fourth-order accurate fractional-step IMEX schemes for the incompressible Navier-Stokes equations on moving overlapping grids. *Comput Methods Appl Mech Eng*. 2020;366:113040.
42. DeCaria V, Schneier M. An embedded variable step IMEX scheme for the incompressible Navier-Stokes equations. *Comput Methods Appl Mech Eng*. 2021;376:113661.
43. Braess D, Verfurth R. A posteriori error estimators for the Raviart-Thomas element. *SIAM J Numer Anal*. 1996;33(6):2431-2444.
44. Ainsworth M, Coyle J. Hierarchic finite element bases on unstructured tetrahedral meshes. *Int J Numer Methods Eng*. 2003;58(14):2103-2130.

45. Guo B, Babuska I, Atluri SN. The h-p version of the finite element method. I: the basic approximation results. *Comput Mech*. 1986;1:203-220.
46. Babuska I, Gui W. The h, p and h-p versions of the finite element method in 1 dimension. Part III. The adaptive h-p version. *Numer Math*. 1986;49:659-684.
47. Fuentes F, Keith B, Demkowicz L, Nagaraj S. Orientation embedded high order shape functions for the exact sequence elements of all shapes. *Comput Math Appl*. 2015;70(4):353-458.
48. Dörfler W, Heuveline V. Convergence of an adaptive hp-finite element strategy in one space dimension. *Appl Numer Math*. 2007;57(10):1108-1124.
49. Kaczmarczyk Ł, Ullah Z, Lewandowski K, et al. MoFEM: an open source, parallel finite element library. *J Open Source Softw*. 2020.
50. Tautges TJ. MOAB-SD: integrated structured and unstructured mesh representation. *Eng Comput*. 2004;20:286-293.
51. Balay S, Gropp WD, McInnes LC, Smith BF. Efficient management of parallelism in object oriented numerical software libraries. In: Arge E, Bruaset AM, Langtangen HP, eds. *Modern Software Tools in Scientific Computing*. Birkhäuser Press; 1997.
52. Abhyankar S, Brown J, Constantinescu EM, Ghosh D, Smith BF, Zhang H. PETSc/TS: a modern scalable ODE/DAE solver library; 2018. arXiv preprint arXiv:1806.01437.
53. Göktepe S, Kuhl E. Computational modeling of cardiac electrophysiology: a novel finite element approach. *Int J Numer Methods Eng*. 2009;79(2):156-178.
54. Mimura M, Tohma M. Dynamic coexistence in a three-species competition-diffusion system. *Ecolog Complex*. 2015;21:215-232.
55. Ainsworth M. A posteriori error estimation for lowest order Raviart-Thomas mixed finite elements. *SIAM J Sci Comput*. 2008;30(1):189-204.
56. Lloyd CM, Yu T. CellML model repository. In: Werner D, Olaf W, Kwang-Hyun C, Hiroki Y, eds. *Encyclopedia of Systems Biology*. Springer; 2013:376-378.
57. Mimura M, Kan-on Y. Dynamic coexistence in a three-species competition-diffusion system. *Predat Mediat Coexist Segregat Struct*. 1986;18:129-155.
58. Brunton SL, Proctor JL, Kutz JN. Discovering governing equations from data by sparse identification of nonlinear dynamical systems. *Proc Natl Acad Sci*. 2016;113(15):3932-3937.
59. Kennedy CA, Carpenter MH. Higher-order additive Runge-Kutta schemes for ordinary differential equations. *Appl Numer Math*. 2019;136:183-205.

How to cite this article: Wakeni MF, Aggarwal A, Kaczmarczyk Ł, et al. A *p*-adaptive, implicit-explicit mixed finite element method for diffusion-reaction problems. *Int J Numer Methods Eng*. 2022;123(14):3237-3263. doi: 10.1002/nme.6967

APPENDIX A. STANDARD FORMULATION

The standard weak problem is defined as

find $m_i \in H^1(\Omega)$, satisfying the boundary conditions (3), such that

$$\frac{\mathrm{d}}{\mathrm{d}t}(v,\ m_i)_\Omega + (\nabla v,\ \boldsymbol{D}_i \nabla m_i)_\Omega = (v,\ \overline{h}_i)_{\Gamma_E} + \ell_i(v), \qquad \forall v \in H^1_{0N}(\Omega), \tag{A1}$$

where $H^1_{0N}(\Omega)$ is a subspace of $H^1(\Omega)$ that contains functions whose trace on Γ_N vanish. Here, it should be noted that the test function v is time-independent.

The functional $\ell_i : H^1(\Omega) \rightarrow \mathrm{I\,R}$ is defined by

$$\ell_i(v) := (f_i,\ v)_\Omega. \tag{A2}$$

The pairings $(\cdot,\ \cdot)_\Omega$ and $(\cdot,\ \cdot)_{\Gamma_{N/E}}$ represent the standard L^2 inner products over the domain Ω and the boundary Γ_N or Γ_E, respectively.

As can be seen from Equation (A1), the boundary condition (4) is incorporated into the weak form, while Equation (3) is enforced as a constraint on the trial solutions. Thus, for the standard formulation, (4) is a natural boundary condition and (3) is an essential boundary condition.

APPENDIX B. SOME OF THE COMMONLY USED IMEX SCHEMES IN THE LITERATURE

- IMEX schemes based on the backward differentiation formula (BDF)

$$\begin{aligned}
\text{Second-order} \quad & \alpha_0 = 1/2,\ \alpha_1 = -2,\ \alpha_2 = 3/2,\\
& \beta_0 = 0,\ \beta_1 = 0,\ \beta_2 = 1,\\
& \gamma_0 = -1,\ \gamma_1 = 2,\\
\text{Third-order} \quad & \alpha_0 = 1/24,\ \alpha_1 = -1/8,\ \alpha_2 = -7/8,\ \alpha_3 = 23/24,\\
& \beta_0 = 1/16,\ \beta_1 = -5/16,\ \beta_2 = 15/16,\ \beta_3 = 5/16,\\
& \gamma_0 = 3/8,\ \gamma_1 = -5/4,\ \gamma_2 = 15/8.
\end{aligned}$$

- The second-order Crank-Nicholson–Adams-Bashforth scheme

$$\begin{aligned}
& \alpha_0 = 0,\ \alpha_1 = -1,\ \alpha_2 = 1,\\
& \beta_0 = 0,\ \beta_1 = 1/2,\ \beta_2 = 1/2,\\
& \gamma_0 = -1/2,\ \gamma_1 = 3/2.
\end{aligned}$$

- The second-order additive Runge–Kutta (RK-IMEX) scheme[59]

$$\begin{aligned}
& \alpha_0 = -1,\ \alpha_1 = 0,\ \alpha_2 = 1\\
& \beta_0 = 1,\ \beta_1 = 0,\ \beta_2 = 1\\
& \gamma_0 = 0,\ \gamma_1 = 2,
\end{aligned}$$